This is a preprint, the final version is subject to change, of the American Mineralogist (MSA)
Cite as Authors (Year) Title. American Mineralogist, in press.
DOI: https://doi.org/10.2138/am-2020-7316

Decoupled water and iron enrichments in the cratonic mantle: a study on peridotite xenoliths from Tok, SE Siberian Craton

Luc S. Doucet[1,2*], Yongjiang Xu (徐永江)[3], Delphine Klaessens[2,4], Hejiu Hui (惠鹤九)[3], Dmitri A. Ionov[5,6] and Nadine Mattielli[2]

[1]*Earth Dynamics Research Group, The Institute for Geoscience Research (TIGeR), Curtin University WA 6845, Australia*

[2]*Laboratoire G-Time, Département Géosciences, Environnement et Société, Université Libre de Bruxelles, 1050 Brussels, Belgium*

[3] *State Key Laboratory for Mineral Deposits Research & Lunar and Planetary Science Institute, School of Earth Sciences and Engineering, Nanjing University, Nanjing 210023, China*

[4] *CRPG, UMR 7358 CNRS - Université de Lorraine, 54501 Vandœuvre-lès-Nancy, France*

[5]*Géosciences Montpellier, UMR-CNRS 5243, Université de Montpellier, 34095 Montpellier, France*

[6] *Guangzhou Institute of Geochemistry, Chinese Academy of Sciences, 510640 Guangzhou, China*

corresponding author: luc.serge.doucet@gmail.com

This is a preprint, the final version is subject to change, of the American Mineralogist (MSA)
Cite as Authors (Year) Title. American Mineralogist, in press.
DOI: https://doi.org/10.2138/am-2020-7316

ABSTRACT (418 words)

Water and iron are believed to be key constituents controlling the strength and density of the lithosphere and, therefore, play a crucial role in the long-term stability of cratons. On the other hand, metasomatism can modify the water and iron abundances in the mantle and possibly triggers thermo-mechanical erosion of cratonic keels. Whether local or large scale processes control water distribution in cratonic mantle remains unclear, calling for further investigation. Spinel peridotite xenoliths in alkali basalts of the Cenozoic Tok volcanic field sampled the lithospheric mantle beneath the southeastern margin of the Siberian Craton. The absence of garnet-bearing peridotite amongst the xenoliths, together with voluminous eruptions of basaltic magma, suggests that the craton margin, in contrast to the central part, lost its deep keel. The Tok peridotites experienced extensive and complex metasomatic reworking by evolved, Ca-Fe-rich liquids that transformed refractory harzburgite to lherzolite and wehrlite. We used polarized Fourier transform infrared spectroscopy (FTIR) to obtain water content in olivine, orthopyroxene (opx), and clinopyroxene (cpx) of 14 Tok xenoliths. Olivine, with a water content of 0-3 ppm H_2O, was severely degassed, probably during emplacement and cooling of the host lava flow. Orthopyroxene (49-106 ppm H_2O) and clinopyroxene (97-300 ppm H_2O) are in equilibrium. The cores of the pyroxene grains, unlike olivine, experienced no water loss due to dehydration or addition attributable to interaction with the host magma. The water contents of opx and cpx are similar to those from the Kaapvaal, Tanzania and North China cratons, but the Tok opx has less water than previously studied opx from the central Siberian craton (Udachnaya, 28-301 ppm; average 138 ppm). Melting models suggest that the water contents of Tok peridotites are higher than in melting residues, and argue for a post-melting (metasomatic) origin.

Moreover, the water contents in opx and cpx of Tok peridotites are decoupled from iron enrichments or other indicators of melt metasomatism (e.g., CaO and P_2O_5). Such decoupling is not seen in the Udachnaya and Kaapvaal peridotites but is similar to observations on Tanzanian peridotites. Our data suggest that iron enrichments in the southeastern Siberian craton mantle preceded water enrichment. Pervasive and large-scale, iron enrichment in the lithospheric mantle may strongly increase its density and initiate a thermo-magmatic erosion. By contrast, the distribution of water in xenoliths is relatively “recent” and was controlled by local

metasomatic processes that operate shortly before the volcanic eruption. Hence, water abundances in minerals of Tok mantle xenoliths appear to represent a snapshot of water in the vicinity of the xenolith source regions.

KEYWORD: peridotite, water, lithospheric mantle, stability, FTIR

INTRODUCTION

The longevity and the stability of the oldest continental domains (also known as 'cratons') are commonly attributed to the presence of a buoyant, cold and "dry" layer in their lithospheric mantle (Boyd, 1989; Hirth et al., 2000; Peslier et al., 2010). This layer is composed of residual peridotites formed by high degrees of melt extraction, responsible for iron- and water-depletion. Such cratonic peridotites are less dense (Herzberg and Rudnick, 2012) and more viscous (Dixon et al., 2004; Hirth et al., 2000) than the surrounding asthenosphere, made up of fertile peridotites richer in iron and containing more water. The cratonic keel is thus physically isolated from the convective mantle and preserved from delamination, providing its longevity (Jordan, 1978; O'Neill et al., 2008; Sleep, 2003).

Studies on cratonic mantle xenoliths worldwide show that most of these peridotites experienced metasomatic re-enrichment in incompatible elements (Carlson et al., 2005; Ionov et al., 2010; Pearson et al., 1995a; Shimizu et al., 1997; Simon et al., 2003), which is often associated with deformation (Boyd and Mertzman, 1987; Ionov et al., 2017). This post-formation modification of the cratonic keel may lead to its erosion (or rejuvenation) (Foley, 2008; Lee et al., 2011; Liu et al., 2019), which may affect either the entire keel, like in the North China Craton (Gao et al., 2002; Griffin et al., 1998; Menzies et al., 2007; Rudnick et al., 2004), or the cratonic margins, like in the Siberian craton (Ionov et al., 2005a; Ionov et al., 2005b), the Colorado Plateau (Lee et al., 2001), the Tanzanian craton (Lee and Rudnick, 1999; Rudnick et al., 1994) and cratons in Greenland (Bernstein et al., 1998; Bernstein et al., 2007).

At least three processes may cause or facilitate the destruction of cratonic keels: (1) convective removal driven by shear stress imposed by mantle flow in the asthenosphere (Cooper and Conrad, 2009; King, 2005), (2) rheological weakening through hydration of the mantle lithosphere by ingress of melt or fluids (Dasgupta et al., 2007; Li et al., 2008) and (3) thermo-magmatic erosion due to enrichment in Fe and heating during modal metasomatism (also referred to as "refertilization") (Foley, 2008). Iron and water appear to be key constituents controlling the stability and the longevity of the lithospheric mantle because they strongly affect its density and strength, respectively.

Water in the mantle primarily resides in nominally anhydrous minerals (NAMs) such as olivine, pyroxenes, and garnet (Asimow and Langmuir, 2003; Bell and Rossman, 1992; Hermann et al., 2007; Hirth and Kohlstedt, 1996; Kovács et al., 2012; Kovacs et al., 2010). Water enters these anhydrous minerals, typically as protons (H^+) bonded to structural oxygen in intrinsic crystal defects (Bell and Rossman, 1992; Rossman, 1996; Smyth et al., 1991). Olivine tends to be stronger if its water content decreases (Mackwell et al., 1985), which may explain why cratonic roots remain strong and resistant for billions of years (Dixon et al., 2004; King, 2005; Mackwell et al., 1985; Peslier, 2010; Pollack, 1986).

The notion of craton-wide dehydration has been questioned by recent studies of water distribution in the cratonic mantle. Water content in minerals shows a clear correlation with metasomatism, especially with iron enrichment, but this correlation seems to be related to local processes (Doucet et al., 2014; Hui et al., 2015; Peslier et al., 2010; Peslier et al., 2012). In the case of the Kaapvaal craton, the enrichment in water is limited to the shallow parts of the cratonic lithosphere (Peslier et al., 2010; Peslier et al., 2012). For the Siberian craton, the water enrichment occurs above the lithosphere-asthenosphere boundary, in laterally-limited regions, probably near shear zones. Water enrichment is associated with modal metasomatism and iron enrichment (Doucet et al., 2014), possibly triggered by asthenospheric volatile-rich silicate melts (Berkesi et al., 2019). By contrast, the water enrichment in the Tanzanian craton is limited to highly-metasomatized peridotites sampled by the Labait volcano (Hui et al., 2015). The North China Craton exhibits elevated water content (Li et al., 2015; Xia et al., 2017) probably caused by metasomatism by aqueous fluids that were likely introduced by subduction (review by Liu et al., 2019). Even if the distribution of water in the cratonic mantle indeed strongly affects the long-term stability of continents (Pollack, 1986), this distribution and the related processes need to be better constrained.

In this study, we report the water content of olivine, orthopyroxene (opx) and clinopyroxene (cpx) of 14 peridotite xenoliths from the Tokinsky Stanovik volcanic field (Tok), located in the Aldan shield on the southeastern (SE) margin of the Siberian craton (Fig. 1). The xenoliths are well-characterized spinel peridotites, some of which experienced pervasive iron enrichment and modal metasomatism shortly before the eruption of host basalts (Ionov et al., 2005a; Ionov et al., 2005b). The absence of garnet-facies peridotite among the Tok

xenoliths confirms the geophysical data suggesting the lost of the deep keel beneath the SE margin of the Siberian craton (Priestley and Debayle, 2003), in contrast to the central Siberian craton where the lithosphere-asthenosphere boundary is 220 km deep according to both xenolith studies (Boyd et al., 1997; Ionov et al., 2010) and geophysical data (Priestley and Debayle, 2003).

The new water data, obtained in this study by polarized FTIR, are compared with the data from an FTIR-study on the spinel and garnet peridotites from the Udachnaya kimberlite in the central Siberian craton (Doucet et al., 2014) to provide an overview of the distribution of water in the lithospheric mantle of the Siberian Craton. The water content in olivine, opx, and cpx are examined in light of available data on the chemical compositions of bulk rocks and minerals to constrain the processes controlling the distribution of water in the cratonic mantle. Finally, the effects of water and iron on the longevity and local erosion of the Siberian craton and the implications of these results for cratons, in general, are reviewed.

GEOLOGICAL SETTING

Neoproterozoic to Paleozoic sediments and Permian-Triassic flood basalts cover the Siberian craton, except for the Anabar and Aldan shields in its northern and south-eastern parts (Fig. 1), where gneisses and granulites with ages up to 3.0–3.6 billion years (Ga) are exposed (Jahn et al., 1998; Nutman et al., 1992; Paquette et al., 2017; Zonenshain et al., 1990). The Archean and Paleoproterozoic blocks amalgamated in the mid-Proterozoic (1.8–2.0 Ga) (Rosen et al., 2005). The oldest Re-Os ages for mantle xenoliths from the Siberian craton are 3.3 Ga (Pearson et al., 1995a; Pearson et al., 1995b), but Re-Os and Lu-Hf data suggest that the main components of the lithospheric mantle formed in two stages about 2.8 Ga and 2.0 Ga (Doucet et al., 2015; Ionov et al., 2015a; Ionov et al., 2015b).

The Aldan shield is the largest area of exposed Archean and Paleoproterozoic (3.6–1.9 Ga) crustal rocks on the Siberian craton (Frost et al., 1998; Jahn et al., 1998; Nutman et al., 1992). The shield is made up of two blocks, the Aldan in the north and the Stanovoy in the south. An area in the eastern Stanovoy Range is called Tokinsky Stanovik and is made of Quaternary alkali basaltic rocks with Ar-Ar ages of 0.59–0.28 Ma (Rasskazov

et al., 2000). Mantle xenoliths in this area are hosted by the basaltic lavas, by contrast with those from the central craton, where they occur in kimberlites.

SAMPLE OVERVIEW

The peridotite xenoliths from Tok are spinel harzburgites, lherzolites, and wehrlites (Fig. 2 and Table 1). Detailed petrographic and geochemical studies of these xenoliths (Ionov et al., 2005a; Ionov et al., 2005b) indicate that the lithospheric mantle beneath Tok first experienced high degrees of melt extraction (up to 25–40%) and then large-scale metasomatic re-working, erasing the geochemical signatures of initial melting events and imparting signatures of enriched melts/fluids in the majority of the samples (Ionov et al., 2006a). Upward migration of mafic silicate melts mainly produced this extensive reworking, followed by the percolation of low-temperature, alkali-rich melts and fluids (Ionov et al., 2006a). Chromatographic fractionation and fractional crystallization of the melts strongly enriched the host peridotite in light (L) rare earth elements (REE) close to the percolation front and dramatically changed the chemical composition of the initial liquids, which progressively evolved from high-T basaltic melts to low-T, alkali-rich silicate and then CO_2- and P_2O_5-rich derivatives (Ionov et al., 2006a). During thermal relaxation of the metasomatic system to ambient geotherm (‘‘retrograde’’ metasomatism), the percolation front migrated downwards. Small-volume residual fluids were trapped, and crystallized volatile-rich accessory minerals such as apatite (F, Cl-rich; up to 1000 ppm H_2O), amphibole (up to 2 to 4 wt.% H_2O) and phlogopite (up to 5 wt.% H_2O) (Ionov et al., 2006a). Shortly before the entrainment of the xenoliths into Quaternary basaltic magma, fluids with low water activity (e.g., due to low H_2O/CO_2) migrated through the lithospheric mantle section triggering the breakdown of hydrous amphibole and phlogopite into anhydrous assemblages and the formation of whitlockite (an anhydrous, halogen-poor and Ca–Mg-rich phosphate) (Ionov et al., 2006b).

Tok peridotites are subdivided in two rock series based on their petrography, modal abundances, Mg# [$Mg/(Mg+Fe)_{at}$] and trace element signatures (Ionov et al., 2005a; Ionov et al., 2005b) (Table 1 and supplementary data 1):

(1) The lherzolite-harzburgite (LH) series groups "normal" (in terms of Mg# and modal composition) fertile to refractory rocks, which are melt extraction residues with relatively low FeO (7.4–9.0 wt.%) and a Mg# ≥ 0.89 (Fig. 3 and 4). The LH series rocks in this study include seven harzburgites, one cpx-poor lherzolite (9510-16) and one fertile lherzolite (9506-2) (Table 1 and Fig. 2). The majority of the LH rocks are variably metasomatized refractory melting residues that have low heavy (H) REE abundances and show consistent gradual enrichments from HREE to LREE. Their LREE patterns are commonly La-enriched in particular for phosphate-bearing samples.

(2) The lherzolite-wehrlite (LW) series is composed of rocks with low Mg# (<0.89), high modal olivine (72–84 wt.%), cpx (7–22 wt.%), and cpx/opx ratios. This series was produced by the reaction of refractory residual peridotites with evolved, Fe-rich (Mg# = 0.6–0.7), silica-undersaturated melts at high melt/rock ratios. This metasomatic process caused replacement of opx by cpx (Fig. 3) and Fe (±Ca, ± trace element) enrichments (Fig. 4c) (Ionov et al., 2005a; Ionov et al., 2005b). The LW series peridotites have lower Mg# than the LH series rocks: 0.829–0.889 for the opx-poor lherzolites and 0.839–0.868 for the wehrlites (Table 1 and Fig. 4a). They have HREE and middle (M) REE abundances five times higher than the refractory LH series rocks (Fig. 5a). Light REE abundances in the LH and LW rock series partly overlap (Fig. 5a).

Both LH and LW series rocks have higher HREE (e.g., Yb in Fig. 5) than refractory peridotites from orogenic (e.g., Horoman Massif, Takazawa et al., 2000) and cratonic settings (e.g., spinel and garnet peridotites from Udachnaya, Ionov et al., 2010) and generally plot above the melting trend in Al_2O_3 vs. Yb plots (Fig. 5b), defined using trace element modelling for non-modal fractional melting of a spinel peridotite with the primitive mantle composition (Doucet et al., 2013). We modelled the partition coefficient between opx and cpx ($D^{cpx/opx}$) following the method of Liang et al. (2013). The measured and predicted $D^{cpx/opx}$ are in good agreement, indicating that REE are in equilibrium between opx and cpx (Fig. 6) in the LH and LW series peridotites. Therefore, opx and cpx are chemically equilibrated and unaffected by host basaltic magma.

The Os-Hf-Sr-Nd isotope study on the spinel peridotites from Tok suggests that, before being highly metasomatized, the lithospheric mantle beneath the SE margin of the Siberian craton formed between 2.8 and

2.0 Ga, i.e., at about the same time as the central and the north-eastern parts of the craton (Doucet et al., 2015; Ionov et al., 2015a; Ionov et al., 2015b).

To sum up, the petrographic and geochemical data of the Tok xenoliths indicate extensive metasomatic re-working of their original residual "protoliths" in two stages: (1) iron enrichments and replacement of opx by cpx in the LW series rocks, produced by the interaction of the protolith with evolved silicate melts; (2) precipitation of fine-grained interstitial materials containing phosphates and alkali feldspar, both in the LH and LW suites, by the migration of water-poor, CO_2-rich fluids through the host peridotite (Ionov et al., 2006a; Ionov et al., 2006b). Overall, the uppermost mantle beneath the SE margin of the Siberian craton may be one of the most strongly metasomatized continental mantle domains worldwide.

METHODS

Sample preparation

Fresh material from xenolith cores (0.1–1 kg) was crushed to <1–2 mm between two hydraulically driven wear-resistant tungsten carbide plates. Gem-quality (i.e., the purest crystals without cracks and inclusions) olivine, opx and cpx, preferably unbroken crystals, were handpicked from sieved >1 mm size fraction for olivine (15–67 per mineral) and 0.6–1 mm for pyroxene (20-40 grains per mineral) under a binocular microscope. The mineral grains were set in epoxy before being polished on two parallel surfaces at the Département de Géologie de l'Université Jean Monnet in Saint-Etienne (France) and at the State Key Laboratory for Mineral Deposits Research of Nanjing University (China). The thickness of the double-polished mineral grains determined with a Mitutoyo digimatic micrometer ranges from 90 to 916 μm (±1 μm). The polished sections were placed in a desiccator before FTIR analyses to eliminate potential surface water.

Fourier Transform Infrared spectroscopy (FTIR)

A continuum infrared microscope in combination with a Nicolet iS50 FTIR at Nanjing University (China) was used to analyze water in olivine and pyroxene. The crystallographic orientation of each polished mineral grain was determined using interference figures under a petrographic microscope. Areas of 30 × 30 to 80 × 80

μm^2 were measured under transmission mode in the wavenumber range of 7000–650 cm^{-1} with a resolution of 4 cm^{-1} and 256 scans. A wire-grid Zn-Se infrared polarizer rotated parallel to each principal axis of the oriented mineral grain was used during FTIR analyses. Each analysis was performed in a pre-dried air environment to minimize interference from ambient atmospheric water vapor. Cross-sections were measured to assess the homogeneity of hydrogen distribution within the grain. Typically, at least one new background spectrum was collected every two hours.

The spectra were normalized to a thickness of 1 cm to be compared with each other and with literature data. The baseline was manually corrected using the Omnic© software. The total integrated absorbance ($\boldsymbol{A_{tot}}$), corresponding to the sum of areas integrated beneath the O-H bands with the vector of the incident infrared light parallel to three principal axes (E//α, E//β, and E//γ), was used to calculate water concentration in each mineral according to the following expression of the Beer-Lambert law:

$$\boldsymbol{C_{H_2O}} = \frac{\boldsymbol{A_{tot}}}{\boldsymbol{I'}},$$

where $\boldsymbol{C_{H_2O}}$ is water concentration (in ppm by weight H_2O), and $\boldsymbol{I'}$ is the integral specific absorption coefficient, which is characteristic of the mineral composition (in ppm^{-1} cm^{-2}). The absorption coefficient used for olivine was I' = 5.32 ± 0.34 ppm^{-1} cm^{-2} between 3800 and 3400 cm^{-1} (Group 1) and 2.22 ± 0.1 ppm^{-1} cm^{-2} between 3400 and 3100 cm^{-1} (Group 2) (Bell et al., 2003), for opx was I' = 15.6 ± 0.94 ppm^{-1} cm^{-2} between 3650 and 2600 cm^{-1} (Bell et al., 1995), and for cpx was I' = 7.09 ± 0.32 ppm^{-1} cm^{-2} between 3650 and 3000 cm^{-1} (Bell et al., 1995). For each mineral of one sample, at least two grains were analyzed to obtain the total integrated absorbance ($\boldsymbol{A_{tot}}$).

FTIR SPECTRA AND OH ABSORBANCE

Absorption bands due to O–H vibrations in olivine and pyroxene of the 14 Tok peridotite xenoliths are located between 3650 and 3100 cm^{-1} and 3650 and 2600 cm^{-1} respectively (supplementary data 2). These spectra are similar to the published OH spectra for olivine and pyroxene in kimberlite-hosted mantle xenoliths from the Siberian craton (Doucet et al., 2014; Matsyuk and Langer, 2004), the Kaapvaal craton (Bell et al., 2003; Peslier

et al., 2010; Peslier et al., 2008), the Ontong Java Plateau (Demouchy et al., 2015), and the Tanzanian craton (Hui et al., 2015). Olivine in the majority of the Tok samples has barely detectable OH bands at 3572 and 3525 cm^{-1}, and 3707 and 3683 cm^{-1}, and could correspond to nano-inclusions of Ti-clinohumite and serpentine respectively (Khisina and Wirth, 2008; Khisina et al., 2008; Kitamura et al., 1987; Koch-Müller et al., 2006; Matsyuk and Langer, 2004; Miller et al., 1987; Mosenfelder et al., 2006). However, such nano-inclusions are undetectable under an optical microscope. The OH absorbance at 3525 cm^{-1} could also be related to intrinsic Ti-defects in olivine (Tollan et al., 2018). In olivine, Ti^{3+} or Ti^{4+} can substitute Mg^{2+} in the octahedral site, and the charge can be balanced by H^{+} replacing Si^{4+}, creating the Ti-clinohumite point defect (Jollands et al., 2016). Titanium being highly incompatible in olivine ($D^{ol/melt}$<0.01, McKenzie and O'Nions, (1991)), the incorporation of Ti in olivine from refractory peridotite can only occur during metasomatism. The contribution of the nano-inclusions remains controversial, but the low alteration of samples (loss on ignition <0.05 wt.%) suggests that these inclusions might have been formed in a mantle environment (Khisina and Wirth, 2008).

The opx have OH bands at 3600, 3565, 3525, and 3440 cm^{-1} (Fig. 7d-f). The cpx have OH bands at 3630, 3525 and 3440 cm^{-1} (Fig. 7g-i). The OH band located at ~3525 cm^{-1} is similar to natural samples from various tectonic settings (Bonadiman et al., 2009; Demouchy et al., 2015; Denis et al., 2018; Peslier et al., 2002). The available experimental work suggests that substitution mechanisms can explain OH bands above 3400 cm−1. In that case, the structural hydroxyl is linked to trivalent cations in the pyroxene structure (Stalder, 2004; Stalder and Skogby, 2002) such as aluminum, sodium and chromium (Aubaud et al., 2004; Bromiley and Keppler, 2004; Hauri et al., 2006; Mierdel and Keppler, 2004; Rauch and Keppler, 2002; Stalder, 2004; Stalder and Skogby, 2002; Tenner et al., 2009). However, the absence of correlation between Al^{IV}, Al^{VI}, Na, Cr and water content in the pyroxene (supplementary data 1) makes any band attribution to specific lattice defect difficult (Peslier et al., 2012). On the other hand, the absence of OH bands at ~3675–3695 cm^{-1}, generally attributed to nano-inclusions of amphibole (Della Ventura et al., 2007; Kovács et al., 2012), suggests that all water has been detected as hydroxyl in intrinsic defects.

The majority of opx has homogenous flat core profiles, excluding the lower absorbance at rims (Fig. 8), and cpx (except cpx from 9510-19) have uniform water content. The cpx from sample 9519-19 has lower abundance at the rim (Fig. 8d), but the difference between the core and rim is limited and close to the uncertainties. The opx with diffusion profiles exhibits much more significant variations between the core and rim (Fig 8a–c). In order to convert the total integrated absorption into H_2O concentrations, we used absorption coefficients from Bell et al. (2003) for olivine and Bell et al. (1995) for pyroxene. We do, however, acknowledge that there remains uncertainty as to the correct choice of absorption coefficient, particularly for olivine (for discussions, see Kovacs et al. (2010); Withers et al. (2012);Demouchy and Bolfan-Casanova (2016); Tollan et al. (2018)), and therefore also provide the total integrated absorbances in Table 1.

The concentrations in the mineral cores are 0–3 ppm H_2O for olivine, 49–106 ppm H_2O for opx, and 97–300 ppm H_2O for cpx (Table 1). The olivine and pyroxene data show that olivine is not in equilibrium with opx and cpx (Fig.9a,b) with $D^{opx/ol}$ and $D^{cpx/ol}$ ranges of 33–374 and 16–822 respectively while the experimental equilibrium range is 3.5–12.2 ($D^{opx/ol}$) (Demouchy et al., 2017; Hauri et al., 2006) and 3.3–33 ($D^{cpx/ol}$) (Novella et al., 2014; Tenner et al., 2009). On the other hand, opx and cpx appear to be in equilibrium (Fig.9c) with $D^{cpx/opx}$ from 1 to 3 with an average of 2, in line with experimental values ranging from 1.2 to 3.5 ($D^{cpx/opx}$) (Hauri et al., 2006; Kovács et al., 2012).

DISCUSSION

Preservation of mantle water content in olivine and pyroxenes

Water content in NAMs is often disturbed during magmatic ascent because hydrogen diffuses rapidly through NAMs at magmatic temperatures (T > 800°C) (Demouchy, 2010; Demouchy and Mackwell, 2003; Kohlstedt and Mackwell, 1998; Mackwell and Kohlstedt, 1990). Host magma, such as continental alkali basalts, may contain up to ~4 wt.% H_2O (Dixon et al., 2002; Dixon et al., 1988; Hochstaedter et al., 1990; Simons et al., 2002; Sisson and Layne, 1993; Stolper and Newman, 1994; Wallace, 2005; Xia et al., 2016) and could

potentially add water to the xenolith. Alternatively, the xenoliths could lose hydrogen via dehydration during decompression and a decrease of water activity (Demouchy et al., 2006; Demouchy and Mackwell, 2006b; Marshall et al., 2018; Patkó et al., 2019) (Demouchy et al., 2006; Demouchy and Mackwell, 2006a; Ingrin and Blanchard, 2006; Peslier and Luhr, 2006; Peslier et al., 2008). This phenomenon may even cause partial or complete dehydration of the grains resulting in no detectable water (Denis et al., 2018; Tian et al., 2017). Therefore, it is essential to establish to what extent measured water concentrations in olivine and pyroxenes may reflect equilibrium mantle concentrations, and this can be done using two approaches. The first is to measure H in profiles across individual grains to determine whether concentration gradients are present and whether they are induced by diffusive loss (or gain) of H. The second is to compare inter-mineral water distribution coefficients with experimental equilibrium water partitioning studies.

The olivine absorbance in thick double-polished grain mounts (>500 μm) is barely above FTIR detection limits, and olivine is not in equilibrium with coexisting pyroxenes, whereas the cores of opx and cpx are equilibrated with each other which indicates water loss in olivine. By contrast, the majority of opx and cpx from xenolith 9510-19 shows water loss at grain edges, but flat absorbance profiles in cores and uniform absorbance values in the cores of different grains. Our data suggest that water had time to diffuse out of olivine and opx but not (or very limited) in cpx, which is in line with recent studies (Tian et al., 2017). Therefore, it is crucial to investigate the effects of diffusion in mineral grains to explore the distribution of water. We model the water loss in olivine and opx using the 1D-diffusion modeling of Peslier et al. (2008), using the equation of Shewmon (1983) (supplementary data 3) and parameters of (Demouchy and Mackwell, 2006a; Stalder and Skogby, 2003; Tian et al., 2017). We assumed a chemical diffusion of H by mobility of metal vacancies, the only mechanism for which diffusion in olivine and opx is significantly faster than cpx and probably the dominant process that controls water diffusion in mantle minerals (Tian et al., 2017; Tollan et al., 2018) (Table 2 and 3 of supplementary data 2). The best fit to the opx data is obtained using the water concentrations measured in the cores as initial water concentrations and diffusion time during 19 days at 900˚C, two days at 1000˚C and 6h at 1100˚C (Fig. 8a). Water diffusion at temperatures above 1200˚C is not well constrained by experimental studies

298 (Tian et al., 2017). The water profiles cannot be reproduced by assuming 25% higher initial water content. We
299 also modelled the water dehydration in olivine at temperatures ranging from 900˚C to 1100˚C for the same
300 diffusion time (19 days, two days, and 6h) (Fig. 8c,d). The initial (pre-dehydration) water concentration in
301 olivine was estimated following the method of Warren and Hauri (2014) using theoretical pyroxene/olivine
302 partition coefficients ($D^{cpx/ol}$ and $D^{opx/ol}$) (Table 2). The average estimated water concentration in olivine is 24 ±
303 13(1σ) ppm. The olivine is degassed to <1 ppm after 19 days at 900˚C, two days at 1000˚C and 6h at 1100˚C
304 (Fig. 8c,d), which suggests that dehydration of olivine and opx may occur between 900˚C (similar to equilibrium
305 temperatures of the xenoliths) and >1100˚C, but also relatively by rapidly to not to affect water in the cpx. At
306 high temperatures (>1100˚C), water diffuses 1-2 orders of magnitude faster in olivine than in opx and up to 10
307 orders of magnitude faster in olivine than in cpx (Demouchy and Bolfan-Casanova, 2016; Ferriss et al., 2016;
308 Ingrin and Blanchard, 2006; Stalder and Behrens, 2006; Stalder et al., 2007; Stalder and Skogby, 2007; Tian et
309 al., 2017; Woods et al., 2000; Xu et al., 2019), and two orders of magnitude faster in opx than in cpx (Tian et al.,
310 2017). On the other hand, water diffusion in cpx is still too fast to avoid partial loss if dehydration occurs at
311 mantle depths (Ferriss et al., 2016; Tian et al., 2017; Xu et al., 2019). Therefore, water diffusion should occur at
312 a sufficiently high temperature to dehydrate olivine and opx edges, but slow enough to preserve the water in the
313 cores of opx and the cpx. Moreover, the shape of the majority of the cpx FTIR spectra in this study (Fig. 7)
314 shows the predominance of OH absorbance at 3630 cm^{-1} defined by Patkó et al. (2019) as “type 1 spectra”. The
315 cpx generally have two intense bands at ~3630 and 3525 cm^{-1} and type 1 spectra is defined when absorption
316 intensity values at ~3630 cm^{-1} dominate. Patkó et al. (2019) show that cpx with type 1 spectra have higher
317 maximum and average water content, and concluded that cpx with type 1 spectra are likely to represent the
318 original conditions, presumably under high water activity. The type 1 spectra of cpx from Tok t suggests that the
319 water content in pyroxenes has been preserved from eruptive processes. In addition, the presence of dry olivine
320 suggests a slow rate of high-temperature annealing (Patkó et al., 2019).

321 The Tok xenoliths were collected in thick alkali basalt lava flows away from eruption centers, which cover
322 210 km^2 in the region; the presence of hawaiites among the volcanic rocks suggests large amounts of hot

(>1000˚C, probably >1200˚C) magma produced (Ionov et al., 2005b). Altogether, the water diffusion profiles in minerals, the water equilibrium between the opx and cpx cores, and field evidence indicate that the transport of the Tok xenoliths in hot host magmas followed by rapid cooling is consistent with dehydration of the xenoliths during the eruption and emplacement of the lava. The effect of the eruption, emplacement, and cooling on the water content of the minerals is in agreement with Li abundances and δ^7Li disequilibria between olivine and pyroxenes attributed to the cooling in thick lava flow (Ionov and Seitz, 2008). Hence, we posit that cpx is the most robust recorder of water content in mantle xenoliths hosted in lava flows.

Water in orthopyroxene and clinopyroxene – melting vs. metasomatism

Partial melting and water content. The tectonic settings responsible for the formation of cratons are still debated, but it is generally accepted that the cratonic mantle lithosphere under ancient continental cores underwent at least 30–40% of melt extraction (Bernstein et al., 1998; Boyd, 1989; Boyd et al., 1997; Doucet et al., 2012; Ionov et al., 2010; Kopylova et al., 1999; Lee, 2006; Pearson and Wittig, 2008; Simon et al., 2007). These melting events occurred during the Archean or early in the Proterozoic (Carlson et al., 1999; Doucet et al., 2015; Ionov et al., 2015a; Ionov et al., 2015b; Pearson et al., 1995a; Wiggers de Vries et al., 2013; Wittig et al., 2010) and must have left behind dry, water-depleted residues (Aubaud et al., 2004; Aubaud et al., 2008; Grant et al., 2006; Grant et al., 2007; Hauri et al., 2006; Tenner et al., 2009). To investigate the links between the distribution of water in the lithospheric mantle of Tok and the melting processes, we modeled the water content of melting residues assuming that water behaves as an incompatible element (Hellebrand et al., 2002; Johnson et al., 1990; Shaw, 1970) (Table 4 of supplementary data 1). We simulated two types of melting: non-modal fractional melting and batch melting (Shaw, 1970) using the partition coefficients of Tenner et al. (2009) for melting at 3GPa (supplementary data 3 and 4). In the first series of modelling, we use the water estimate for the primitive mantle (1100 ppm H_2O) as the initial water content of the melting source (Bell and Rossman, 1992; Palme and O'Neill, 2003). The non-modal fractional melting model produces "dry" bulk-rock residues and pyroxenes (both < 0.1 ppm H_2O) after only 6–7% of melt extraction at 3 GPa. By contrast, in the batch melting

model, the residue still contains about 20 ppm H_2O in bulk rock, 30 ppm H_2O in opx, and 30 ppm H_2O in cpx even after 25% melting.

In the second series of modeling, the water content estimate for a water-depleted source (180 ppm H_2O), similar to the source region of mid-ocean ridge basalts (MORB), is used as the initial water content of the fertile peridotite source (Danyushevsky et al., 2000; Dixon et al., 1988; Michael, 1995; Michael, 1988; Sobolev and Chaussidon, 1996). After 4–5% of fractional melting, the bulk residue becomes "dry" (< 0.1 ppm of water). Even if the partition coefficient of Sokol et al. (2013) between olivine and melt is applied ($D_{H_2O}^{ol/melt}$ ~0.003, which is 5 times higher than the partition coefficient of Tenner et al. (2009), $D_{H_2O}^{ol/melt}$ ~0.0006), the water content in opx and cpx of <0.1 ppm H_2O is obtained. The residue contains <10 ppm H_2O in opx and cpx after 25 % of batch melting, which is lower than the degrees of melting commonly inferred for cratonic peridotites, i.e. 30 to 40% (Lee et al., 2011). This value is lower than the water content in Tok pyroxenes as well.

The opx from the Tok xenoliths in this study contain up to 106 ppm H_2O and the cpx up to 300 ppm. Our modelling shows that such water concentrations cannot be residual after partial melting, especially at high melting degrees (30–40%) and thus was added to the xenoliths after melt extraction. This inference agrees with the absence of a correlation between water content in the pyroxenes and melts depletion indices in this study. Metasomatism generally erases the record of partial melting for incompatible elements in residues and may control the distribution of water in the cratonic mantle (Doucet et al., 2014; Hui et al., 2015; Peslier and Bizimis, 2015; Peslier et al., 2012; Selway et al., 2014).

Metasomatism and water content. Recent studies on water distribution in cratonic mantle reveal positive correlations between water in minerals and metasomatism indices (see review by Peslier et al., 2017). For example, the water content in garnets correlates with TiO_2 concentration in garnet from the in Kaapvaal (South Africa) and Udachnaya (central Siberia) xenoliths (Doucet et al., 2014; Peslier et al., 2012). Water content in cpx from Kaapvaal peridotites correlate with its trace element compositions. The water content in olivine from Udachnaya peridotites is generally higher with xenoliths with high olivine Mg# (Fig. 10a), high

372 modal cpx (Fig. 10b) (Doucet et al., 2014). These correlations indicate that ~~the~~ water has been added to the
373 lithospheric mantle by melts or fluids derived from the asthenosphere (Bell and Rossman, 1992; Doucet et al.,
374 2014; Peslier et al., 2012).

375 The mantle beneath Tok experienced a pervasive and complex metasomatic transformation, first by evolved
376 mafic melts to form the LW series rocks containing accessory hydrous phases, then by "dry" fluids that affected
377 refractory peridotites of both the LH and LW series. The first metasomatic event encompassed the whole
378 lithospheric mantle section ''sampled'' by the xenoliths (likely in the depth range of 40–60 km) (Ionov et al.,
379 2005a; Ionov et al., 2005b), and locally erased the geochemical record of previous melting events. It was not
380 directly related to the late Cenozoic basaltic volcanism, but could probably be associated with an earlier
381 magmatic event. The melts/fluids of this first major metasomatic event, which enriched some Tok peridotites in
382 Fe and massively crystallized new cpx, may be similar to metasomatic agents responsible for modal
383 metasomatism of Udachnaya garnet peridotites (Doucet et al., 2013). This similarity and the presence of
384 accessory water-bearing minerals in the LW Tok series suggest significant water content in the mantle beneath
385 Tok during this event and are in apparent contradiction with the "normal" water content measured in Tok
386 pyroxenes. The first metasomatic episode could be related to a significant tectono-magmatic event at the SE
387 margin of the Siberian craton in the late-Mesozoic to early-Cenozoic (Zonenshain et al., 1990), that involved
388 alkali magmatism and graben formation and possibly associated with subduction in the adjacent paleo-Pacific
389 oceanic basin. The combination of these two events may have resulted in the delamination of the lower
390 lithospheric mantle beneath Tok, and supplied the heat and melts/fluids for the main metasomatic event in the
391 shallow lithospheric mantle (Ionov et al., 2005a; Ionov et al., 2005b).

392 Following this first major metasomatism event, small-scale late-stage metasomatic episodes continued in
393 the lithospheric mantle beneath Tok until the eruption of the basaltic magmas that host the xenoliths. Melts
394 and/or fluids with a low water activity (e.g., due to low H_2O/CO_2) migrated through the lithospheric mantle
395 shortly before the entrainment of the xenoliths into the host magma and their ascent to the surface. Evidence for
396 this migration of CO_2-rich, water-poor melts/fluids is recorded in the peridotite xenoliths as follows (Ionov et

al., 2006a; Ionov et al., 2006b): (i) the presence of quenched cryptocrystalline materials with empty vesicles and of fine-grained aggregates (alkali feldspar, Ti-rich oxides, micro-phenocrysts of olivine, cpx, spinel and phosphates); (ii) the breakdown of ‘‘hydrous’’ amphibole and phlogopite into ‘‘anhydrous’’ assemblages (e.g., Ba-Ti-rich silicates); and (iii) the formation of whitlockite group minerals (anhydrous, halogen-poor and Ca–Mg-rich phosphates, mainly the Na-rich merrillite). These ‘‘dry’’ melts/fluids affected almost every xenolith from Tok, both from the LW and from the LH series. They were chemically different from the fluids that previously crystallized volatile-rich minerals and probably came from a genetically distinct source, possibly related to the Quaternary alkali basaltic magmatism (Ionov et al., 2006a; Ionov et al., 2006b).

The absence of correlations (i.e., decoupling) between the water content in opx and cpx with modal cpx and FeO (Fig. 10c–f), and other indices of melt metasomatism in Tok peridotites, suggest that the water abundances are either (i) not related to the first metasomatic episode that produced iron and cpx enrichments, or (ii) were modified by later metasomatic events. The water abundances in opx and cpx are similar to those in the cratonic mantle, and opx–cpx equilibrium indicates no significant water loss. These observations-suggest that either (i) the opx and cpx were not (or little) affected by the dry metasomatism or (ii) they were dehydrated by the dry metasomatism and have been enriched by later events.

In comparison, strongly metasomatized xenoliths with low water content in NAMs (1–39 ppm H_2O in olivine with an average of 10 ppm H_2O) also occur on the Tanzanian craton (Hui et al., 2015). The Tanzanian craton has been affected by a mantle plume, which has significantly reworked the cratonic lithospheric mantle (Lee and Rudnick, 1999). The Tanzanian peridotites experienced Fe-enrichments (bulk FeO up to 10 wt.%; olivine Mg# down to 89) and precipitation of cpx (up to 14% with an average of 4–5%), probably caused by relatively water-poor (<1 wt.% H_2O), yet LREE- and Fe-enriched plume-derived melts (Hui et al., 2015).

The potential metasomatic agents responsible for water addition to the Tok peridotites have an estimated average water content between 0.6 ± 0.4 and 1.0 ± 0.9 wt.% H_2O (O'Leary et al., 2010) (Table 2), using the temperature of equilibration and the potential temperature of the metasomatic agent in the mantle (i.e., 1200˚C; Ionov et al. (2005b)) (Table 1). Such water content is similar to those in mid-ocean ridge basalts (~0.1-0.5 wt.%

422 H_2O) and ocean island basalts (~0.1-1 wt.% H_2O), but generally lower than for other mantle-derived melts i.e.,
423 back-arc basalts (~0.5-2.1 wt.% H_2O), island arc basalts (~2-8 wt.% H_2O) and continental flood basalts (~3-7
424 wt.% H_2O) (Xia et al., 2016 and reference therein). Overall, the decoupling between water and iron suggests that
425 (i) the iron enrichments that likely caused the thermo-mechanical erosion of the southeastern margin of the
426 Siberian craton were not accompanied by water enrichment; or (ii) the Fe enrichment event was accompanied by
427 water enrichment, but overprinted by subsequent processes, such as "dry" metasomatism by water-poor
428 melts/fluids.

429 **Water controls on the stability of the cratonic lithospheric mantle**

430 To investigate the role of water and iron in the stability of cratonic lithosphere, we modeled the viscosity
431 (Fig. 11) in the Tok peridotite mantle as a function of depth, water content in olivine and whole-rock major
432 element compositions following the methods of Li et al. (2008) and Peslier et al. (2010). (Table 5 of
433 supplementary data 1). We used the average estimated water concentration in Tok olivine, i.e., 24 ± 13 (1σ) ppm
434 (see above). Viscosity estimates for our Tok samples are compared here to those for the lithospheric mantle
435 beneath Udachnaya in the central Siberian craton (η_{eff}=8.4 x 10^{16} to 1.9 x 10^{28} Pa·s^{-1}) (Doucet et al., 2014), the
436 Kaapvaal craton (η_{eff}=4.8 x 10^{17} to 1.7 x 10^{24} Pa·s^{-1}) (Peslier et al., 2010), the Tanzanian craton (η_{eff}=4.8 x 10^{17}
437 to 1.7 x 10^{24} Pa·s^{-1}) (Hui et al., 2015) and a range of viscosity estimates for the asthenosphere (η_{eff}=5.4 x 10^{17} to
438 2.7 x 10^{25} Pa·s^{-1} and d=3.33g·cm^{-3}) (Fleming et al., 2007; Larsen et al., 2005; Pollitz et al., 1998; Sjöberg et al.,
439 2000). On the one hand, the estimated viscosity range of Tok peridotites (LH and LW series) of 1.7 x 10^{28} to 1.9
440 x 10^{31} Pa·s^{-1} tends to be significantly higher than the average viscosity estimated for the asthenosphere of 3.7 x
441 10^{18} Pa·s^{-1} (Fig. 11). On the other, the viscosity range of the Tok peridotites is narrower than that calculated for
442 Udachnaya peridotites. The latter, however, is so significant that it may indicate the superposition of multiple
443 processes. The viscosity range for the Tanzanian craton is narrower than that for the central Siberian craton, with
444 less extreme high values. At depths <100 km, the Tanzanian peridotite xenoliths yield a viscosity range (η_{eff}=4.8
445 x 10^{17} to 1.7 x 10^{24} Pa·s^{-1}) lower than for the Tok peridotites because the former contain more water (1 to 39

446 ppm H_2O in olivine with an average of 10 ppm H_2O). However, Hui et al. (2015) showed that the low viscosities
447 calculated for the Tanzanian peridotites result from the combination of low water content with higher
448 equilibration temperatures (930-1410 °C) and a hotter geotherm (50 MW/m^2 vs. 41 MW/ m^2 for most other
449 cratons (Lee and Rudnick, 1999)), consistent with the presence of a mantle plume beneath the Tanzanian craton
450 (Aulbach et al., 2008; Lee and Rudnick, 1999; Pik et al., 2006; Selway et al., 2014), and indicate that the most
451 significant influence on viscosity estimates is exerted by mantle temperature (e.g., Karato, 2010). Regarding the
452 viscosities of the Tok peridotites, the relatively low temperature of equilibrium (800-1000˚C with an average of
453 950˚C) and the low water content in olivine (24 ± 13(1σ) ppm) make the lithospheric mantle beneath the SE
454 margin of the Siberian craton viscous and therefore resistant.
455

456 **IMPLICATIONS**

457 This work reports the water content in the nominally anhydrous minerals of the peridotite xenoliths from
458 Tok, representative of the lithospheric mantle beneath the SE Siberian craton. Olivine is mostly "dry" due to
459 dehydration; the opx rims are also affected by the dehydration, but their cores preserve their mantle water
460 concentrations. The cpx are not affected by dehydration and are in equilibrium with water in the opx cores.
461 Altogether, our data indicate that the dehydration occurred at high temperature (900 to >1000˚C) in a short time
462 (several days) during emplacement and cooling, and demonstrate that cpx is the most robust recorder of water
463 abundances in mantle xenoliths hosted in lava flows.

464 The lithospheric mantle beneath the SE margin of the Siberian craton has lost its cratonic keel,
465 supposedly by thermo-magmatic erosion triggered by large-scale Fe enrichment metasomatic events involving
466 mafic melts, which simultaneously heated up and metasomatized the lithospheric mantle. The initial (pre-
467 dehydration) olivine (24 ± 13(1σ) ppm), opx (74 ± 34(1σ) ppm) and cpx (146 ± 75(1σ) ppm) water content of
468 the peridotite xenoliths from Tok are similar to those in olivine in diamond inclusions (Jean et al., 2016) and
469 minerals from refractory spinel peridotites from the central Siberian craton (Doucet et al., 2014), and similar to

un-metasomatized cratonic minerals (Peslier et al., 2017). All of this suggests that the SE margin of the Siberian craton lithospheric mantle is relatively "dry" with an average bulk water content of 41 ± 13(1σ) ppm.

The decoupling between the water abundances in mantle minerals and metasomatic indices suggests that the large-scale metasomatism responsible for the Fe enrichments was asynchronous with water enrichments or has been overprinted by later processes. Our findings question the notion of "wet" metasomatism by large scale water-rich asthenospheric melts, proposed in previous studies (Doucet et al., 2014; Li et al., 2018; Peslier et al., 2012), as a valid explanation for cratonic mantle delamination (Li et al., 2015; Xia et al., 2017). Instead, we infer that water abundance variations are spatially localized and limited in time and probably result from local, spatially restricted melting and metasomatism events in the mantle (Peslier et al., 2017).

ACKNOWLEDGMENTS

LSD thanks Colette Guilbaud for preparing high-quality double-polished grain mounts at the Université J Monnet. We thank I. Kovacs, P. Tollan, and Q. Xia for helpful comments and suggestions that improve the previous version of this manuscript. Financial support was provided to LSD by the Belgium F.R.S.-FNRS "mandat Chargé de Recherche" (n°1.B.102.14F). DAI acknowledges the Visiting Scientist fellowships within the CAS (Chinese Academy of Sciences) President's International Fellowship Initiative (PIFI) in 2017-19 (Grant No. 2017VCA0009). HH acknowledges support from the Natural Science Foundation of China (41590623 and 41573055).

REFERENCES

Ashchepkov, I.V., Ntaflos, T., Vladykin, N.V., Ionov, D.A., Kuligin, S.S., Malygina, L.V., Pokhilenko, L.N., Logvinova, A.M., Mityukhin, S.I., Palessky, S.V., Khmelnikova, O.S., and Rotman, A.Y. (2010) Deep seated xenoliths from the phlogopite-bearing brown breccia of Udachnaya pipe. In N.V. Vladykin, Ed. Deep-Seated Magmatism, its Sources and Plumes, p. 164-186. Vinogradov Institute of Geochemistry, Russian Academy of Science, Irkutsk.

Asimow, P.D., and Langmuir, C.H. (2003) The importance of water to oceanic mantle melting regimes. Nature, 421(6925), 815 - 820.

Aubaud, C., Hauri, E.H., and Hirschmann, M.M. (2004) Hydrogen partition coefficients between nominally anhydrous minerals and basaltic melts. Geophysical Research Letters, 31(20), L20611.

Aubaud, C., Hirschmann, M., Withers, A., and Hervig, R. (2008) Hydrogen partitioning between melt, clinopyroxene, and garnet at 3 GPa in a hydrous MORB with 6 wt% H2O. Contributions to Mineralogy and Petrology, 156(5), 607-625.

Aulbach, S., Rudnick, R., and McDonough, W. (2008) Li-Sr-Nd isotope signatures of the plume and cratonic lithospheric mantle beneath the margin of the rifted Tanzanian craton (Labait). Contributions to Mineralogy and Petrology, 155(1), 79-92.

Bell, D.R., Ihinger, P.D., and Rossman, G.R. (1995) Quantitative analysis of trace OH in garnet and pyroxenes. American Mineralogist, 80(5-6), 465-474.

Bell, D.R., and Rossman, G.R. (1992) Water in Earth`s Mantle: The Role of Nominally Anhydrous Minerals. Science, 255(5050), 1391-1396.

Bell, D.R., Rossman, G.R., Maldener, J., Endisch, D., and Rauch, F. (2003) Hydroxide in olivine: A quantitative determination of the absolute amount and calibration of the IR spectrum. Journal of Geophysical Research, 108(B2), 2105.

Berkesi, M., Czuppon, G., Szabó, C., Kovács, I., Ferrero, S., Boiron, M.-C., and Peiffert, C. (2019) Pargasite in fluid inclusions of mantle xenoliths from northeast Australia (Mt. Quincan): evidence of interaction with asthenospheric fluid. Chemical Geology, 508, 182-196.

Bernstein, S., Kelemen, P.B., and Brooks, C.K. (1998) Depleted spinel harzburgite xenoliths in Tertiary dykes from East Greenland: restites from high degree melting. Earth and Planetary Science Letters, 154(1-4), 219-233.

Bernstein, S., Kelemen, P.B., and Hanghoj, K. (2007) Consistent olivine Mg# in cratonic mantle reflects Archean mantle melting to the exhaustion of orthopyroxene. Geology, 35(5), 459-462.

Bonadiman, C., Hao, Y., Coltorti, M., Dallai, L., Faccini, B., Huang, Y., and Xia, Q. (2009) Water contents of pyroxenes in intraplate lithospheric mantle. European Journal of Mineralogy, 21(3), 637-647.

Boyd, F.R. (1989) Compositional distinction between oceanic and cratonic lithosphere. Earth and Planetary Science Letters, 96, 15-26.

Boyd, F.R., and Mertzman, S.A. (1987) Composition and structure of the Kaapvaal lithosphere, Southern Africa. In B.O. Mysen, Ed. Magmatic Processes: Physicochemical Principles, 1, p. 3-12. Geochemical Society Special Publications **1**.

Boyd, F.R., Pokhilenko, N.P., Pearson, D.G., Mertzman, S.A., Sobolev, N.V., and Finger, L.W. (1997) Composition of the Siberian cratonic mantle: evidence from Udachnaya peridotite xenoliths. Contribution to Mineralogy and Petrology, 128, 228-246.

Bromiley, G., and Keppler, H. (2004) An experimental investigation of hydroxyl solubility in jadeite and Na-rich clinopyroxenes. Contributions to Mineralogy and Petrology, 147(2), 189-200.

Carlson, R.W., Pearson, D.G., Boyd, F.R., Shirey, S.B., Irvine, G., Menzies, A.H., and Gurney, J.J. (1999) Re-Os systematics of lithosphere peridotites: implications for lithosphere formation and preservation. In J.J. Gurney, J.L. Gurney, M.D. Pascoe, and S.H. Richardson, Eds. Proceedings 7th International Kimberlite Conference, 1, p. 99-108. RedRoof Design, Cape Town.

Carlson, R.W., Pearson, D.G., and James, D.E. (2005) Physical, chemical, and chronological characteristics of continental mantle. Reviews in Geophysics, 43(RG1001), doi:10.1029/2004RG000156.

Cooper, C., and Conrad, C.P. (2009) Does the mantle control the maximum thickness of cratons? Lithosphere, 1(2), 67-72.

Danyushevsky, L.V., Eggins, S.M., Fallon, T.J., and D.M., C. (2000) H2O Abundance in Depleted to Moderately Enriched Mid-ocean Ridge Magmas; Part I: Incompatible Behaviour, Implications for Mantle Storage, and Origin of Regional Variations. Journal of Petrology, 41(8), 1329-1364.

Dasgupta, R., Hirschmann, M.M., and Smith, N.D. (2007) Water follows carbon: CO2 incites deep silicate melting and dehydration beneath mid-ocean ridges. Geology, 35(2), 135-138.

Della Ventura, G., Oberti, R., Hawthorne, F.C., and Bellatreccia, F. (2007) FTIR spectroscopy of Ti-rich pargasites from Lherz and the detection of O2− at the anionic O3 site in amphiboles. American Mineralogist, 92(10), 1645-1651.

Demouchy, S. (2010) Hydrogen diffusion in spinel grain boundaries and consequences for chemical homogenization in hydrous peridotite. Contributions to Mineralogy and Petrology, 160(6), 887-898.

Demouchy, S., and Bolfan-Casanova, N. (2016) Distribution and transport of hydrogen in the lithospheric mantle: A review. Lithos, 240, 402-425.

Demouchy, S., Ishikawa, A., Tommasi, A., Alard, O., and Keshav, S. (2015) Characterization of hydration in the mantle lithosphere: Peridotite xenoliths from the Ontong Java Plateau as an example. Lithos, 212-215, 189-201.

Demouchy, S., Jacobsen, S.D., Gaillard, F., and Stern, C.R. (2006) Rapid magma ascent recorded by water diffusion profiles in mantle olivine. Geology, 34(6), 429-432.

Demouchy, S., and Mackwell, S. (2003) Water diffusion in synthetic iron-free forsterite. Physics and Chemistry of Minerals, 30(8), 486-494.

Demouchy, S., and Mackwell, S. (2006a) Mechanisms of hydrogen incorporation and diffusion in iron-bearing olivine. Physics and Chemistry of Minerals, 33(5), 347.

-. (2006b) Mechanisms of hydrogen incorporation and diffusion in iron-bearing olivine. Physics and Chemistry of Minerals, 33(5), 347-355.

Demouchy, S., Shcheka, S., Denis, C.M., and Thoraval, C. (2017) Subsolidus hydrogen partitioning between nominally anhydrous minerals in garnet-bearing peridotite. American Mineralogist: Journal of Earth and Planetary Materials, 102(9), 1822-1831.

Denis, C.M., Demouchy, S., and Alard, O. (2018) Heterogeneous hydrogen distribution in orthopyroxene from veined mantle peridotite (San Carlos, Arizona): Impact of melt-rock interactions. Lithos, 302, 298-311.

Dixon, J.E., Dixon, T.H., Bell, D.R., and Malservisi, R. (2004) Lateral variation in upper mantle viscosity: role of water. Earth and Planetary Science Letters, 222(2), 451-467.

Dixon, J.E., Leist, L., Langmuir, C., and Schilling, J.-G. (2002) Recycled dehydrated lithosphere observed in plume-influenced mid-ocean-ridge basalt. Nature, 420(6914).

Dixon, J.E., Stolper, E., and Delaney, J.R. (1988) Infrared spectroscopic measurements of CO2 and H2O in Juan de Fuca Ridge basaltic glasses. Earth and Planetary Science Letters, 90(1), 87-104.

Doucet, L., Ionov, D., and Golovin, A. (2013) The origin of coarse garnet peridotites in cratonic lithosphere: new data on xenoliths from the Udachnaya kimberlite, central Siberia. Contributions to Mineralogy and Petrology, 165(6), 1225-1242.

Doucet, L.S., Ionov, D.A., and Golovin, A.V. (2015) Paleoproterozoic formation age for the Siberian cratonic mantle: Hf and Nd isotope data on refractory peridotite xenoliths from the Udachnaya kimberlite. Chemical Geology, 391(0), 42-55.

Doucet, L.S., Ionov, D.A., Golovin, A.V., and Pokhilenko, N.P. (2012) Depth, degrees and tectonic settings of mantle melting during craton formation: inferences from major and trace element compositions of spinel harzburgite xenoliths from the Udachnaya kimberlite, central Siberia. Earth and Planetary Science Letters, 359–360, 206-218.

Doucet, L.S., Peslier, A.H., Ionov, D.A., Brandon, A.D., Golovin, A.V., Goncharov, A.G., and Ashchepkov, I.V. (2014) High water contents in the Siberian cratonic mantle linked to metasomatism: An FTIR study of Udachnaya peridotite xenoliths. Geochimica et Cosmochimica Acta, 137(0), 159-187.

Ferriss, E., Plank, T., and Walker, D. (2016) Site-specific hydrogen diffusion rates during clinopyroxene dehydration. Contributions to Mineralogy and Petrology, 171(6), 55.

Fleming, K., Martinec, Z., and Wolf, D. (2007) Glacial-isostatic Adjustment and the Viscosity Structure Underlying the Vatnajökull Ice Cap, Iceland. Pure and Applied Geophysics, 164(4), 751-768.

Foley, S.F. (2008) Rejuvenation and erosion of the cratonic lithosphere. Nature Geoscience, 1(8), 503-510.

Frost, B.R., Avchenko, O.V., Chamberlain, K.R., and Frost, C.D. (1998) Evidence for extensive Proterozoic remobilisation of the Aldan shield and implications for Proterozoic plate tectonic reconstructions of Siberia and Laurentia. Precambrian Research, 89, 1-23.

Gao, S., Rudnick, R.L., Carlson, R.W., McDonough, W.F., and Liu, Y.-S. (2002) Re-Os evidence for replacement of ancient mantle lithosphere beneath the North China craton. Earth and Planetary Science Letters, 198(3-4), 307-322.

Grant, K., Kohn, S., and Brooker, R. (2006) Solubility and partitioning of water in synthetic forsterite and enstatite in the system MgO-SiO2-H2O±AL2O3. Contributions to Mineralogy and Petrology, 151(6), 651-664.

Grant, K.J., Kohn, S.C., and Brooker, R.A. (2007) The partitioning of water between olivine, orthopyroxene and melt synthesised in the system albite–forsterite–H2O. Earth and Planetary Science Letters, 260(1-2), 227-241.

Griffin, W.L., Zhang, A., O'Reilly, S.Y., and Ryan, C.G. (1998) Phanerozoic evolution of the lithosphere beneath the Sino-Korean craton. In M.J.F. Flower, S.-L. Chung, C.-H. Lo, and T.Y. Lee, Eds. Mantle Dynamics and Plate Interactions in East Asia, 27, p. 107-126. Amer. Geophys. Union, Geodynamics Series Vol. 27, Washington D.C.

Hauri, E.H., Gaetani, G.A., and Green, T.H. (2006) Partitioning of water during melting of the Earth's upper mantle at H2O-undersaturated conditions. Earth and Planetary Science Letters, 248(3-4), 715-734.

Hellebrand, E., Snow, J.E., Hoppe, P., and Hofmann, A.W. (2002) Garnet-field melting and late-stage refertilization in 'residual' abyssal peridotites from the Central Indian Ridge. Journal of Petrology, 43(12), 2305-2338.

Hermann, J., Fitz Gerald, J., Malaspina, N., Berry, A., and Scambelluri, M. (2007) OH-bearing planar defects in olivine produced by the breakdown of Ti-rich humite minerals from Dabie Shan (China). Contributions to Mineralogy and Petrology, 153(4), 417-428.

Herzberg, C., and Rudnick, R. (2012) Formation of cratonic lithosphere: An integrated thermal and petrological model. Lithos(0).

Hirth, G., Evans, R.L., and Chave, A.D. (2000) Comparison of continental and oceanic mantle electrical conductivity: Is the Archean lithosphere dry? Geochemistry, Geophysics, Geosystems, 1(12), 1030.

Hirth, G., and Kohlstedt, D.L. (1996) Water in the oceanic upper mantle: Implications for rheology, melt extraction and the evolution of the lithosphere. Earth And Planetary Science Letters, 144(1-2), 93-108.

Hochstaedter, A.G., Gill, J.B., Kusakabe, M., Newman, S., Pringle, M., Taylor, B., and Fryer, P. (1990) Volcanism in the Sumisu Rift, I. Major element, volatile, and stable isotope geochemistry. Earth and planetary science letters, 100(1), 179-194.

Hui, H., Peslier, A.H., Rudnick, R.L., Simonetti, A., and Neal, C.R. (2015) Plume-cratonic lithosphere interaction recorded by water and other trace elements in peridotite xenoliths from the Labait volcano, Tanzania. Geochemistry, Geophysics, Geosystems, 16(6), 1687-1710.

Ingrin, J., and Blanchard, M. (2006) Diffusion of Hydrogen in Minerals. Reviews in Mineralogy and Geochemistry, 62(1), 291-320.

Ionov, D.A. (2004) Chemical variations in peridotite xenoliths from Vitim, Siberia: inferences for REE and Hf behaviour in the garnet facies upper mantle. Journal of Petrology, 45(2), 343-367.

Ionov, D.A., Carlson, R.W., Doucet, L.S., Golovin, A.V., and Oleinikov, O.B. (2015a) The age and history of the lithospheric mantle of the Siberian craton: Re-Os and PGE study of peridotite xenoliths xenoliths from the Obnazhennaya kimberlite. Earth and Planetary Science Letters, 418, 108-119.

Ionov, D.A., Chanefo, I., and Bodinier, J.-L. (2005a) Origin of Fe-rich lherzolites and wehrlites from Tok, SE Siberia by reactive melt percolation in refractory mantle peridotites. Contribution to Mineralogy and Petrology, 150(3), 335-353.

Ionov, D.A., Chazot, G., Chauvel, C., Merlet, C., and Bodinier, J.-L. (2006a) Trace element distribution in peridotite xenoliths from Tok, SE Siberian craton: A record of pervasive, multi-stage metasomatism in shallow refractory mantle. Geochimica et Cosmochimica Acta, 70(5), 1231-1260.

Ionov, D.A., Doucet, L.S., and Ashchepkov, I.V. (2010) Composition of the lithospheric mantle in the Siberian craton: New constraints from fresh peridotites in the Udachnaya-East kimberlite. Journal of Petrology, 51(11), 2177-2210.

Ionov, D.A., Doucet, L.S., Carlson, R.W., Golovin, A.V., and Korsakov, A.V. (2015b) Post-Archean formation of the lithospheric mantle in the central Siberian craton: Re–Os and PGE study of peridotite xenoliths from the Udachnaya kimberlite. Geochimica et Cosmochimica Acta, 165, 466-483.

Ionov, D.A., Doucet, L.S., von Strandmann, P.A.P., Golovin, A.V., and Korsakov, A.V. (2017) Links between deformation, chemical enrichments and Li-isotope compositions in the lithospheric mantle of the central Siberian craton. Chemical Geology, 475, 105-121.

Ionov, D.A., Hofmann, A.W., Merlet, C., Gurenko, A.A., Hellebrand, E., Montagnac, G., Gillet, P., and Prikhodko, V.S. (2006b) Discovery of whitlockite in mantle xenoliths: Inferences for water- and halogen-poor fluids and trace element residence in the terrestrial upper mantle. Earth and Planetary Science Letters, 244(1-2), 201-217.

Ionov, D.A., Prikhodko, V.S., Bodinier, J.-L., Sobolev, A.V., and Weis, D. (2005b) Lithospheric mantle beneath the south-eastern Siberian craton: petrology of peridotite xenoliths in basalts from the Tokinsky Stanovik. Contribution to Mineralogy and Petrology, 149(6), 647-665.

Ionov, D.A., and Seitz, H.M. (2008) Lithium abundances and isotopic compositions in mantle xenoliths from subduction and intra-plate settings: mantle sources versus eruption histories. Earth and Planetary Science Letters, 266(3-4), 316-331.

Jahn, B.-M., Gruau, G., Capdevila, R., Cornichet, J., Nemchin, A., Pidgeon, R., and Rudnik, V.A. (1998) Archean crustal evolution of the Aldan Shield, Siberia: geochemical and isotopic constraints. Precambrian Research, 91, 333-363.

Jean, M.M., Taylor, L.A., Howarth, G.H., Peslier, A.H., Fedele, L., Bodnar, R.J., Guan, Y., Doucet, L.S., Ionov, D.A., Logvinova, A.M., Golovin, A.V., and Sobolev, N.V. (2016) Olivine inclusions in Siberian diamonds and mantle xenoliths: Contrasting water and trace-element contents. Lithos, 265, 31-41.

Johnson, K.T.M. (1998) Experimental determination of partition coefficients for rare earth and high-field-strength elements between clinopyroxene, garnet, and basaltic melt at high pressures. Contribution to Mineralogy and Petrology, 133, 60-68.

Johnson, K.T.M., Dick, H.J.B., and Shimizu, N. (1990) Melting in the oceanic upper mantle: An ion probe study of diopsides in abyssal peridotites. Journal of Geophysical Research, 95(B3), 2661-2678.

Jollands, M., Hermann, J., O'Neill, H.S.C., Spandler, C., and Padrón-Navarta, J. (2016) Diffusion of Ti and some divalent cations in olivine as a function of temperature, oxygen fugacity, chemical potentials and crystal orientation. Journal of petrology, 57(10), 1983-2010.

Jordan, T.H. (1978) Composition and development of the continental tectosphere. Nature, 274, 544-548.

Karato, S.-i. (2010) Rheology of the deep upper mantle and its implications for the preservation of the continental roots: A review. Tectonophysics, 481(1,Äì4), 82-98.

Khisina, N., and Wirth, R. (2008) Nanoinclusions of high-pressure hydrous silicate, Mg3Si4O10(OH)2 · nH2O (10Å-phase), in mantle olivine: Mechanisms of formation and transformation. Geochemistry International, 46(4), 319-327.

Khisina, N., Wirth, R., Matsyuk, S., and Koch-Muller, M. (2008) Microstructures and OH-bearing nano-inclusions in "wet" olivine xenocrysts from the Udachnaya kimberlite. European Journal of Mineralogy, 20(6), 1067-1078.

King, S.D. (2005) Archean cratons and mantle dynamics. Earth and Planetary Science Letters, 234(1-2), 1-14.

Kitamura, M., Kondoh, S., Morimoto, N., Miller, G.H., Rossman, G.R., and Putnis, A. (1987) Planar OH-bearing defects in mantle olivine. Nature, 328, 143-145.

Koch-Müller, M., Matsyuk, S., Rhede, D., Wirth, R., and Khisina, N. (2006) Hydroxyl in mantle olivine xenocrysts from the Udachnaya kimberlite pipe. Physics and Chemistry of Minerals, 33(4), 276-287.

Kohlstedt, D.L., and Mackwell, S.J. (1998) Diffusion of Hydrogen and Intrinsic Point Defects in Olivine. Zeitschrift für Physikalische Chemie, 207(Part_1_2), 147-162.

Kopylova, M.G., Russell, J.K., and Cookenboo, H. (1999) Petrology of peridotite and pyroxenite xenoliths from the Jerico kimberlite: Implications for the thermal state of the mantle beneath the Slave craton, Northern Canada. Journal of Petrology, 40(1), 79-104.

Kovács, I., Green, D.H., Rosenthal, A., Hermann, J., O'neill, H.S.C., Hibberson, W.O., and Udvardi, B. (2012) An experimental study of water in nominally anhydrous minerals in the upper mantle near the water-saturated solidus. Journal of Petrology, 53(10), 2067-2093.

Kovacs, I., O'Neill, H.S.C., Hermann, J., and Hauri, E.H. (2010) Site-specific infrared O-H absorption coefficients for water substitution into olivine. American Mineralogist, 95(2-3), 292-299.

Larsen, C.F., Motyka, R.J., Freymueller, J.T., Echelmeyer, K.A., and Ivins, E.R. (2005) Rapid viscoelastic uplift in southeast Alaska caused by post-Little Ice Age glacial retreat. Earth and Planetary Science Letters, 237(3–4), 548-560.

Lee, C.-T. (2006) Geochemical/petrological constraints on the origin of cratonic mantle. In K. Benn, J.-C. Mareschal, and K.C. Condie, Eds. Archean Geodynamics and Environments, p. 89-114. Amer. Geophys. Union Monograph, Washington.

Lee, C.-T., and Rudnick, R.L. (1999) Compositionally stratified cratonic lithosphere: petrology and geochemistry of peridotite xenoliths the Labait volcano, Tanzania. In J.J. Gurney, J.L. Gurney, M.D. Pascoe, and S.H. Richardson, Eds. Proceedings 7th International Kimberlite Conference, Vol I: The Dawson Volume, p. 503-521. RedRoof Design, Cape Town.

Lee, C.-T., Yin, Q., Rudnick, R.L., and Jacobsen, S.B. (2001) Preservation of ancient and fertile lithospheric mantle beneath southwestern USA. Nature, 411(6833), 69-73.

Lee, C.-T.A., Luffi, P., and Chin, E.J. (2011) Building and Destroying Continental Mantle. Annual Review of Earth and Planetary Sciences, 39(1), 59-90.

Li, P., Scott, J.M., Liu, J., and Xia, Q.-k. (2018) Lateral H2O variation in the Zealandia lithospheric mantle controls orogen width. Earth and Planetary Science Letters, 502, 200-209.

Li, P., Xia, Q.-K., Deloule, E., Chen, H., Gu, X.-Y., and Feng, M. (2015) Temporal variation of H2O content in the lithospheric mantle beneath the eastern North China Craton: Implications for the destruction of cratons. Gondwana Research, 28(1), 276-287.

Li, Z.-X.A., Lee, C.-T.A., Peslier, A.H., Lenardic, A., and Mackwell, S.J. (2008) Water contents in mantle xenoliths from the Colorado Plateau and vicinity: Implications for the mantle rheology and hydration-induced thinning of continental lithosphere. Journal of Geophysical Research, 113, B09210, doi:10.1029/2007JB005540.

Liang, Y., Sun, C., and Yao, L. (2013) A REE-in-two-pyroxene thermometer for mafic and ultramafic rocks. Geochimica et Cosmochimica Acta, 102, 246-260.

Liu, J., Cai, R., Pearson, D.G., and Scott, J.M. (2019) Thinning and destruction of the lithospheric mantle root beneath the North China Craton: A review. Earth Science Reviews, 196, 102873.

Mackwell, S.J., and Kohlstedt, D.L. (1990) Diffusion of Hydrogen in Olivine: Implications for Water in the Mantle. Journal of Geophysical Research, 95(B4), 5079-5088.

Mackwell, S.J., Kohlstedt, D.L., and Paterson, M.S. (1985) The Role of Water in the Deformation of Olivine Single Crystals. Journal of Geophysical Research, 90(B13), 11319-11333.

Marshall, E.W., Lassiter, J.C., and Barnes, J.D. (2018) On the (mis) behavior of water in the mantle: Controls on nominally anhydrous mineral water content in mantle peridotites. Earth and Planetary Science Letters, 499, 219-229.

Matsyuk, S.S., and Langer, K. (2004) Hydroxyl in olivines from mantle xenoliths in kimberlites of the Siberian platform. Contributions to Mineralogy and Petrology, 147(4), 413-437.

McDonough, W.F., and Sun, S.-s. (1995) The composition of the Earth. Chemical Geology, 120, 223-253.

McKenzie, D., and O'Nions, R.K. (1991) Partial melt distributions from inversion of rare earth element concentrations. Journal of Petrology, 32(5), 1021-1091.

Menzies, M., Xu, Y., Zhang, H., and Fan, W. (2007) Integration of geology, geophysics and geochemistry: A key to understanding the North China Craton. Lithos, 96(1-2), 1-21.

Michael, P. (1995) Regionally distinctive sources of depleted MORB: Evidence from trace elements and H2O. Earth and Planetary Science Letters, 131(3–4), 301-320.

Michael, P.J. (1988) The concentration, behavior and storage of H2O in the suboceanic upper mantle: Implications for mantle metasomatism. Geochimica et Cosmochimica Acta, 52, 555-566.

Mierdel, K., and Keppler, H. (2004) The temperature dependence of water solubility in enstatite. Contribution to Mineralogy and Petrology, 148(3), 305-311.

Miller, G.H., Rossman, G.R., and Harlow, G.E. (1987) The natural occurrence of hydroxide in olivine. Physics and Chemistry of Minerals, 14(5), 461-472.

Mosenfelder, J.L., Sharp, T.G., Asimow, P.D., and Rossman, G.R. (2006) Hydrogen Incorporation in Natural Mantle Olivines. Earth's Deep Water Cycle, p. 45-56. American Geophysical Union.

Novella, D., Frost, D.J., Hauri, E.H., Bureau, H., Raepsaet, C., and Roberge, M. (2014) The distribution of H2O between silicate melt and nominally anhydrous peridotite and the onset of hydrous melting in the deep upper mantle. Earth and Planetary Science Letters, 400, 1-13.

Nutman, A.P., Chernyshev, I.V., Baadsgaard, H., and Smelov, A.P. (1992) The Aldan Shield of Siberia, USSR: the age of its Archean components and evidence for widespread reworking in the mid-Proterozoic. Precambrian Research, 54, 195-210.

O'Leary, J.A., Gaetani, G.A., and Hauri, E.H. (2010) The effect of tetrahedral Al3+ on the partitioning of water between clinopyroxene and silicate melt. Earth and Planetary Science Letters, 297(1-2), 111-120.

O'Neill, C.J., Lenardic, A., Griffin, W.L., and O'Reilly, S.Y. (2008) Dynamics of cratons in an evolving mantle. Lithos, 102(1-2), 12-24.

Palme, H., and O'Neill, H.S.C. (2003) Cosmochemical estimates of mantle composition. In R.W. Carlson, Ed. Treatise on Geochemistry. Vol. 2. The Mantle and Core, p. 1-38. Elsevier.

Paquette, J.-L., Ionov, D.A., Agashev, A., Gannoun, A., and Nikolenko, E. (2017) Age, provenance and Precambrian evolution of the Anabar shield from U-Pb and Lu-Hf isotope data on detrital zircons, and the history of the northern and central Siberian craton. Precambrian Research, 301, 134-144.

Patkó, L., Liptai, N., Kovács, I.J., Aradi, L.E., Xia, Q.-K., Ingrin, J., Mihály, J., O'reilly, S.Y., Griffin, W.L., and Wesztergom, V. (2019) Extremely low structural hydroxyl contents in upper mantle xenoliths from the Nógrád-Gömör Volcanic Field (northern Pannonian Basin): Geodynamic implications and the role of post-eruptive re-equilibration. Chemical Geology, 507, 23-41.

Pearson, D.G., Shirey, S.B., Carlson, R.W., Boyd, F.R., Pokhilenko, N.P., and Shimizu, N. (1995a) Re-Os, Sm-Nd, and Rb-Sr isotope evidence for thick Archaean lithospheric mantle beneath the Siberian craton modified by multistage metasomatism. Geochimica et Cosmochimica Acta, 59(5), 959-977.

Pearson, D.G., Snyder, G.A., Shirey, S.B., Taylor, L.A., Carlson, R.W., and Sobolev, N.V. (1995b) Archaean Re-Os age for Siberian eclogites and constraints on Archaean tectonics. Nature, 374, 711-713.

Pearson, D.G., and Wittig, N. (2008) Formation of Archaean continental lithosphere and its diamonds: the root of the problem. Journal of the Geological Society of London, 165(5), 895-914.

Peslier, A.H. (2010) A review of water contents of nominally anhydrous natural minerals in the mantles of Earth, Mars and the Moon. Journal of Volcanology and Geothermal Research, 197(1-4), 239-258.

Peslier, A.H., and Bizimis, M. (2015) Water in Hawaiian peridotite minerals: A case for a dry metasomatized oceanic mantle lithosphere. Geochemistry, Geophysics, Geosystems, 16(4), 1211-1232.

Peslier, A.H., Francis, D., and Ludden, J. (2002) The lithospheric mantle beneath continental margins: melting and melt-rock reaction in Canadian Cordillera xenoliths. Journal of Petrology, 43(11), 2013-2047.

Peslier, A.H., and Luhr, J.F. (2006) Hydrogen loss from olivines in mantle xenoliths from Simcoe (USA) and Mexico: Mafic alkalic magma ascent rates and water budget of the sub-continental lithosphere. Earth and Planetary Science Letters, 242(3-4), 302-319.

Peslier, A.H., Schönbächler, M., Busemann, H., and Karato, S.-I. (2017) Water in the Earth's interior: distribution and origin. Space Science Reviews, 212(1-2), 743-810.

Peslier, A.H., Woodland, A.B., Bell, D.R., and Lazarov, M. (2010) Olivine water contents in the continental lithosphere and the longevity of cratons. Nature, 467(7311), 78-81.

Peslier, A.H., Woodland, A.B., Bell, D.R., Lazarov, M., and Lapen, T.J. (2012) Metasomatic control of water contents in the Kaapvaal cratonic mantle. Geochimica et Cosmochimica Acta, 97(0), 213-246.

Peslier, A.H., Woodland, A.B., and Wolff, J.A. (2008) Fast kimberlite ascent rates estimated from hydrogen diffusion profiles in xenolithic mantle olivines from southern Africa. Geochimica et Cosmochimica Acta, 72(11), 27112722.

Pik, R., Marty, B., and Hilton, D.R. (2006) How many mantle plumes in Africa? The geochemical point of view. Chemical Geology, 226(3-4), 100-114.

Pollack, H.N. (1986) Cratonization And Thermal Evolution Of The Mantle. Earth And Planetary Science Letters, 80(1-2), 175-182.

Pollitz, F.F., Bürgmann, R., and Romanowicz, B. (1998) Viscosity of Oceanic Asthenosphere Inferred from Remote Triggering of Earthquakes. Science, 280(5367), 1245-1249.

Priestley, K., and Debayle, E. (2003) Seismic evidence for a moderately thick lithosphere beneath the Siberian Platform. Geophysical Research Letters, 30(3), 1118.

Rasskazov, S.V., Boven, A., Ivanov, A.V., and Semenova, V.G. (2000) Middle Quaternary volcanic impulse in the Olekma-Stanovoy mobile system: ^{40}Ar-^{39}Ar dating of volcanics from the Tokinsky Stanovik. Tikhookeanskaya Geologiya, 19(4), 19-28 (in Russian).

Rauch, M., and Keppler, H. (2002) Water solubility in orthopyroxene. Contributions to Mineralogy and Petrology, 143(5), 525-536.

Rosen, O.M., Manakov, A.V., and Suvorov, V.D. (2005) The collisional system in the northeastern Siberian craton and a problem of diamond-bearing lithospheric keel. Geotectonics, 39(6), 456-479.

Rossman, G.R. (1996) Studies of OH in nominally anhydrous minerals. Physics and Chemistry of Minerals, 23(4), 299-304.

Rudnick, R.L., Gao, S., Ling, W.-l., Liu, Y.-s., and McDonough, W.F. (2004) Petrology and geochemistry of spinel peridotite xenoliths from Hannuoba and Qixia, North China craton. Lithos, 77(1-4), 609-637.

Rudnick, R.L., McDonough, W.F., and Orpin, A. (1994) Northern Tanzanian peridotite xenoliths: A comparison with Kaapvaal peridotites and inferences on metasomatic interactions. In H.O.A. Meyer, and O. Leonardos, Eds. Kimberlites, Related Rocks and Mantle Xenoliths. Proceedings 5th Internat. Kimberlite Conf., vol. 1, p. 336-353. CPRM, Brasilia.

Selway, K., Yi, J., and Karato, S.-I. (2014) Water content of the Tanzanian lithosphere from magnetotelluric data: Implications for cratonic growth and stability. Earth and Planetary Science Letters, 388(0), 175-186.

Shaw, D.M. (1970) Trace element fractionation during anatexis. Geochimica et Cosmochimica Acta, 34, 237-243.

Shewmon, P.G. (1983) Diffusion in solid. J. Williams Book Compagny, Jenks, OK.

Shimizu, N., Pokhilenko, N.P., Boyd, F.R., and Pearson, D.G. (1997) Geochemical characteristics of mantle xenoiliths from the Udachnaya kimberlite pipe. Russian Geology and Geophysics, 38(1), 205-217.

Simon, N.S.C., Carlson, R.W., Pearson, D.G., and Davies, G.R. (2007) The origin and evolution of the Kaapvaal cratonic lithospheric mantle. Journal of Petrology, 48(3), 589-625.

Simon, N.S.C., Irvine, G.J., Davies, G.R., Pearson, D.G., and Carlson, R.W. (2003) The origin of garnet and clinopyroxene in "depleted" Kaapvaal peridotites. Lithos, 71(2-4), 289-322.

Simons, K., Dixon, J., Schilling, J.G., Kingsley, R., and Poreda, R. (2002) Volatiles in basaltic glasses from the Easter-Salas y Gomez Seamount Chain and Easter Microplate: Implications for geochemical cycling of volatile elements. Geochemistry, Geophysics, Geosystems, 3(7), 1-29.

Sisson, T.W., and Layne, G.D. (1993) H2O in basalt and basaltic andesite glass inclusions from four subduction-related volcanoes. Earth and Planetary Science Letters, 117(3–4), 619-635.

Sjöberg, L.E., Pan, M., Asenjo, E., and Erlingsson, S. (2000) Glacial rebound near Vatnajökull, Iceland, studied by GPS campaigns in 1992 and 1996. Journal of Geodynamics, 29(1–2), 63-70.

Sleep, N.H. (2003) Survival of Archean cratonal lithosphere. Journal of Geophysical Research: Solid Earth, 108(B6).

Smyth, J.R., Bell, D.R., and Rossman, G.R. (1991) Incorporation of hydroxyl in upper-mantle clinopyroxenes. Nature, 351(6329), 732-735.

Sobolev, A.V., and Chaussidon, M. (1996) H2O concentrations in primary melts from supra-subduction zones and mid-ocean ridges: implications for H2O storage and recycling in the mantle. Earth and Planetary Science Letters, 137, 45-55.

Sokol, A.G., Kupriyanov, I.N., Palyanov, Y.N., Kruk, A.N., and Sobolev, N.V. (2013) Melting experiments on the Udachnaya kimberlite at 6.3–7.5 GPa: Implications for the role of H2O in magma generation and formation of hydrous olivine. Geochimica et Cosmochimica Acta, 101(0), 133-155.

Stalder, R. (2004) Influence of Fe, Cr and Al on hydrogen incorporation in orthopyroxene. European Journal of Mineralogy, 16(5), 703-711.

Stalder, R., and Behrens, H. (2006) D/H exchange in pure and Cr-doped enstatite: implications for hydrogen diffusivity. Physics and Chemistry of Minerals, 33(8), 601-611.

Stalder, R., Purwin, H., and Skogby, H. (2007) Influence of Fe on hydrogen diffusivity in orthopyroxene. European Journal of Mineralogy, 19(6), 899-903.

Stalder, R., and Skogby, H. (2002) Hydrogen incorporation in enstatite. European Journal of Mineralogy, 14(6), 1139-1144.

Stalder, R., and Skogby, H. (2003) Hydrogen diffusion in natural and synthetic orthopyroxene. Physics and Chemistry of Minerals, 30(1), 12-19.
Stalder, R., and Skogby, H. (2007) Dehydration mechanisms in synthetic Fe-bearing enstatite. European Journal of Mineralogy, 19(2), 201-216.
Stolper, E., and Newman, S. (1994) The role of water in the petrogenesis of Mariana trough magmas. Earth and Planetary Science Letters, 121, 293-325.
Streckeisen, A. (1976) To each plutonic rock its proper name. Earth Science Reviews, 12, 1-33.
Takazawa, E., Frey, F.A., Shimizu, N., and Obata, M. (2000) Whole rock compositional variations in an upper mantle peridotite (Horoman, Hokkaido, Japan): Are they consistent with a partial melting process. Geochimica et Cosmochimica Acta, 64(4), 695-716.
Tenner, T.J., Hirschmann, M.M., Withers, A.C., and Hervig, R.L. (2009) Hydrogen partitioning between nominally anhydrous upper mantle minerals and melt between 3 and 5 GPa and applications to hydrous peridotite partial melting. Chemical Geology, 262(1–2), 42-56.
Tian, Z.-Z., Liu, J., Xia, Q.-K., Ingrin, J., Hao, Y.-T., and Christophe, D. (2017) Water concentration profiles in natural mantle orthopyroxenes: A geochronometer for long annealing of xenoliths within magma. Geology, 45(1), 87-90.
Tollan, P.M., O'Neill, H.S.C., and Hermann, J. (2018) The role of trace elements in controlling H incorporation in San Carlos olivine. Contributions to mineralogy and petrology, 173(11), 89.
Wallace, P.J. (2005) Volatiles in subduction zone magmas: concentrations and fluxes based on melt inclusion and volcanic gas data. Journal of Volcanology and Geothermal Research, 140(1), 217-240.
Warren, J.M., and Hauri, E.H. (2014) Pyroxenes as tracers of mantle water variations. Journal of Geophysical Research: Solid Earth, 119(3), 1851-1881.
Wiggers de Vries, D.F., Pearson, D.G., Bulanova, G.P., Smelov, A.P., Pavlushin, A.D., and Davies, G.R. (2013) Re–Os dating of sulphide inclusions zonally distributed in single Yakutian diamonds: Evidence for multiple episodes of Proterozoic formation and protracted timescales of diamond growth. Geochimica et Cosmochimica Acta, 120(0), 363-394.
Withers, A.C., Bureau, H., Raepsaet, C., and Hirschmann, M.M. (2012) Calibration of infrared spectroscopy by elastic recoil detection analysis of H in synthetic olivine. Chemical Geology, 334(0), 92-98.
Wittig, N., Webb, M., Pearson, D.G., Dale, C.W., Ottley, C.J., Hutchison, M., Jensen, S.M., and Luguet, A. (2010) Formation of the North Atlantic Craton: Timing and mechanisms constrained from Re-Os isotope and PGE data of peridotite xenoliths from S.W. Greenland. Chemical Geology, 276(3-4), 166-187.
Woods, S.C., Mackwell, S., and Dyar, D. (2000) Hydrogen in diopside: Diffusion profiles. American Mineralogist, 85(3-4), 480-487.
Xia, Q.-K., Bi, Y., Li, P., Tian, W., Wei, X., and Chen, H.-L. (2016) High water content in primitive continental flood basalts. Scientific Reports, 6, 25416.
Xia, Q.-K., Liu, J., Kovács, I., Hao, Y.-T., Li, P., Yang, X.-Z., Chen, H., and Sheng, Y.-M. (2017) Water in the upper mantle and deep crust of eastern China: concentration, distribution and implications. National Science Review, 6(1), 125-144.
Xu, Y., Tang, W., Hui, H., Rudnick, R.L., Shang, S., and Zhang, Z. (2019) Reconciling the discrepancy between the dehydration rates in mantle olivine and pyroxene during xenolith emplacement. Geochimica et Cosmochimica Acta, 267, 179-195.
Zonenshain, L.P., Kuzmin, M.I., and Natapov, L.M. (1990) Geology of the USSR: a plate tectonic synthesis. 242 p. Amer. Geophys. Union, Geodynamics Ser. 21, Washington, D.C.

FIGURE CAPTIONS

Fig. 1. (a) Location map of the Tok volcanic field (red star) and the Udachnaya kimberlite pipe (blue circle) in the Siberian craton, adapted from Ashchepkov et al. (2010); the insert in the upper right corner shows the

position of the craton in the Russian Federation. Also shown are the Anabar and Aldan shields and main kimberlite fields. (b) A sketch map of Tok basaltic field, eruption center, and mantle xenoliths occurrences alongside the upper river Tok, after Ionov et al. (2005b).

Fig. 2. Modal proportions of olivine and pyroxenes in Tok peridotites in this study (filled symbols) and other available data (empty symbols) (Ionov et al., 2005a; Ionov et al., 2005b). The peridotite types are after Streckeisen (1976): (1) lherzolite, (2) harzburgite, (3) dunite, and (4) wehrlite. Tok peridotite xenoliths are subdivided into two groups, the lherzolite-harzburgite series (LH, green circles) and the lherzolite-wehrlite series (LW, red squares). Dashed contours delimit LH (green) and LW (red) series.

Fig. 3. Co-variation plots of modal olivine vs. clinopyroxene **(a)** and orthopyroxene **(b)** for Tok peridotites (Ionov et al., 2005a; Ionov et al., 2005b) [see Fig. 2. for symbols]. Also shown are Udachnaya spinel (black circles) and garnet peridotites (blue squares) (Doucet et al., 2013; Doucet et al., 2012; Ionov et al., 2010), Horoman peridotites (grey zone; Takazawa et al. (2000)) and primitive mantle (PM) estimates (Johnson, 1998). Red and green arrows show metasomatism trends.

Fig. 4. Co-variation plots of major elements in whole-rock (WR) Tok spinel peridotites (Ionov et al., 2005a; Ionov et al., 2005b): Al_2O_3 vs. Mg# = $[Mg/(Mg+Fe)_{at}]$ **(a)** and FeO_T (total iron) **(b)**; CaO vs. FeO_T **(c)** [see Fig. 2 and 3 for symbols]. Also shown are Udachnaya spinel and garnet peridotites (Doucet et al., 2013; Doucet et al., 2012; Ionov et al., 2010), Horoman peridotites (grey zone; Takazawa et al. (2000)) and primitive mantle estimates (Johnson, 1998). Arrows show melting (bold black curve in **a**) and metasomatism trends.

Fig. 5. (a) Primitive mantle-normalized (McDonough and Sun, 1995) REE patterns of whole-rock LH (green field) and LW (red field) series refractory peridotites from Tok (Ionov et al., 2005a; Ionov et al., 2005b). Also shown are the harzburgites (dot-dashed grey field) and the lherzolites (hatched grey field) from the Horoman

massif (Takazawa et al., 2000). **(b)** Co-variation plot of Al_2O_3 vs. Yb (in ppm) for whole-rock (WR) Tok peridotites (Ionov et al., 2005a; Ionov et al., 2005b) in comparison with trace element modelling for non-modal fractional melting of a spinel peridotite with the primitive mantle composition (Doucet et al., 2013). Also shown are Udachnaya spinel and garnet peridotites (Doucet et al., 2013; Doucet et al., 2012; Ionov et al., 2010), Horoman peridotites (grey zone; Takazawa et al. (2000)) and primitive mantle estimates (Johnson, 1998) [see Fig. 2 and 3 for symbols]. The bold black curve shows the melting trend.

Fig. 6. REE partitioning between orthopyroxene and clinopyroxene ($D^{cpx/opx}$) for Tok peridotites from the LH series (green curves) and LW series (red curves) **(a)** in this study compared to off-craton peridotite from Vitim (blue curves; (Ionov, 2004)) and predicted $D^{cpx/opx}$ (Liang et al., 2013) **(b)**. The comparison between measured $D^{cpx/opx}$ and predicted $D^{cpx/opx}$ for Y, Dy, Sm, and Ce for Tok xenoliths in this study indicates that opx and cpx are in equilibrium **(c)**.

Fig. 7. Representative FTIR spectra along E//α, E//β and E//γ crystallographic axis of olivine **(a,b,c)**, opx **(d,e,f)** and cpx **(g,h,i)** for each sample (LH series in green and LW series in red) in the O-H vibration region from 3800 to 2800 cm^{-1} for olivine and 3800 to 2600 cm^{-1} for pyroxenes. Absorbance plotted for a sample thickness of 1 cm.

Fig. 8. Absorbance area in cm^{-2} the opx from sample 9510-4 **(a)**, 9510-11 **(b)**, 9503-2 **(c)**, and cpx from sample 9508-50 and 9810-19 **(d)**, i.e. area integrated beneath OH bands, vs. distance across minerals grains in µm. The diffusion modelling of H loss uses Eq. (5) from Peslier et al. (2008): hydrogen diffusion models are based on 2-dimension diffusion equations for a sample of finite size surrounded by an infinite medium containing no H (Shewmon, 1983). The H diffusion coefficients (Diff, in $m^2\ s^{-1}$) is assumed to be similar for each axis with 10^{-14} m^2/s at 900°C, 10^{-13} m^2/s at 1000°C and $10^{-12} m^2/s$ at 11000°C (isotropic)(Tian et al., 2017). For each opx in **(a)**, three models are achieved at 900°C with two different initial concentrations: the two first models uses the water

951 content measured in the core of olivine (~2-3 ppm H_2O) (solid curves), and the second one, a water content of
952 25% higher (dashed curves). The two first models are the best fit for the FTIR data revealing that the mantle
953 water content of Tok opx has been preserved in their cores.
954
955 **Fig. 9.** Assessment of equilibrium for water between minerals by comparing ratios of water content measured
956 with partition coefficient measured experimentally. H06, (Hauri et al., 2006); T09, (Tenner et al., 2009); N14,
957 (Novella et al., 2014); D17, (Demouchy et al., 2017).
958
959 **Fig. 10.** Covariation plots of water content in opx and cpx (H_2O in ppm) vs. Mg# in olivine **(a-b)**, modal
960 clinopyroxene **(c-d)** and FeO_T **(e-f)** for Tok (Ionov et al., 2005a; Ionov et al., 2005b) [see Fig. 2 and 3 for
961 symbols]. Also shown are the data for Udachnaya garnet peridotites (Doucet et al., 2013; Doucet et al., 2012;
962 Ionov et al., 2010), primitive mantle estimates (Johnson, 1998), the peridotite xenoliths from the Kaapvaal
963 (yellow field or dot) (Peslier et al., 2010) the Tanzanian cratons (white ellipses or dot) (Hui et al., 2015) and the
964 North China Craton (data compiled by Peslier et al., 2017). For comparison, we also plot the estimated value for
965 the sub-cratonic lithospheric mantle Peslier et al. (2017)
966
967 **Fig. 11.** Effective viscosity (in Pa s) vs. depth (in km and GPa) of peridotite xenoliths from Tok (red field),
968 Udachnaya (blue field) (Doucet et al., 2014), the Kaapvaal (yellow field) (Peslier et al., 2010) and the Tanzanian
969 cratons (empty field) (Hui et al., 2015). The viscosity was calculated for olivine aggregates in dislocation creep
970 with the estimated olivine water content assuming equilibrium with the cpx (Table 2), and using the equation of
971 Li et al. (2008). The grey curve represents the viscosity of the cratonic mantle estimated with a constant water
972 content of 300 ppm. The cratonic geotherm was calculated assuming a heat flow of 40 mW/m^2 following the
973 equation $T = 360.73 + 9.0612\ P - 0.0206\ P^2 + (2.0 \times 10^{-5})\ P^3$, with T in K and P in km. Are also shown the range
974 of the viscosities of the asthenosphere (grey field) (Fleming et al., 2007; Larsen et al., 2005; Pollitz et al., 1998;

975 Sjöberg et al., 2000), the spinel stability field (brown field) and the depth of the lithosphere-asthenosphere

976 boundary (LAB) beneath the central part of the Siberian craton.

This is a preprint, the final version is subject to change, of the American Mineralogist (MSA)
Cite as Authors (Year) Title. American Mineralogist, in press.
DOI: https://doi.org/10.2138/am-2020-7316

Table 1 : Summary of petrological data, and water content in olivine and pyroxenes for Tok xenoliths in this study

	Rock	T (°C)	Mg#	Modal abundances (wt.%)								d	Viscosity	Total integrated absorbance (A_{Tot})				Water contents in minerals and whole-rock							
Sample	Type	Ca-opx	Ol	Ol	Opx	Cpx	Spl	Felds	Ap	Am, Phl	Wh	g.cm^{-3}	Pa.s^{-1}	Ol, G1	Ol, G2	Opx	Cpx	Ol [1]	± *(2σ)*	Ol [2]	± *(2σ)*	Opx	± *(2σ)*	Cpx	± *(2σ)*	WR
Lherzolite-harzburgite (LH) series																										
9501-2	Hzb	910	0.908	78.6	17.2	3.1	0.3	0.7*	0.12			3.34	4.2E+30	0.56	2.6	927	854	0.3	*0.2*	20	*33*	59	*27*	120**	*48*	30
9506-2	Lhz	1001	0.889	53.9	26.3	17.3	2.5					3.35	1.7E+28	3.3	0	933	688	0.6	*0.2*	16	*26*	60	*24*	97	*20*	41
9508-31	Hzb	887	0.911	76.5	16.6	4.8	0.4	1.7*	0.06		tr.	3.33	1.9E+31	1.0	0	870		0.2	*0.1*	22	*0*	56	*22*	/132/	*129*	32
9508-50	Hzb	992	0.907	77.1	17.6	3.6	0.7	0.9*	0.07			3.34	2.1E+28	1.2	0	1340	883	0.2	*0.1*	21	*34*	86	*23*	125	*30*	36
9510-2	Hzb	914	0.912	77.2	16.6	4.3	0.4	1.3*	0.12			3.34	9.2E+29	7.4	1.6	1656	2125	1.5	*0.3*	50	*82*	106	*33*	300**	*57*	69
9510-4	Hzb	926	0.909	79.9	16.0	2.7	0.4	1.0*	0.11			3.34	5.6E+29	4.6	1.1	1631	1688	1.0	*0.9*	40	*65*	105	*17*	238	*53*	55
9510-8	Hzb	950	0.904	79.2	14.9	4.9	0.4	0.6*	0.08			3.35	2.1E+29	4.6	3.0	1169	1086	1.1	*0.7*	26	*42*	75	*25*	153	*42*	39
9510-16	Lhz	957	0.894	76.2	17.4	6.0	0.4					3.35	2.0E+29	3.1	1.3	1283	807	0.7	*0.3*	19	*31*	82	*18*	114	*46*	36
9510-19	Hzb	951	0.907	72.7	22.8	3.4	0.7		0.30		tr.	3.34	3.5E+29	0.90	1.1	1091	701	0.3	*0.1*	17	*27*	70	*13*	99	*28*	31
Lherzolite-wehrlite (LW) series																										
9503-2	Lhz	949	0.890	75.9	5.9	15.2	0.8		0.12	2.1		3.37	3.4E+29	6.8	2.6	765	791	1.5	*0.5*	19	*31*	49	*11*	112**	*30*	34
9510-11	Lhz	920	0.851	78.2	12.6	7.4	0.4	1.1*	0.42			3.45	1.3E+30	2.1	0	935	1221	0.4	*0.1*	29	*47*	60	*14*	172	57	43
9502-1	Wh		0.870	78.3	0.9	19.5	0.3	0.9*	0.15			3.39		3.3	0	n.a.	73	0.6	*0.5*	2	*3*	/6/	*5*	10	*4*	3
9510-1	Wh	964	0.857	71.5	2.9	22.4	1.5	1.6*	0.10			3.40	4.4E+28	1.7	0	n.a.	1864	0.3	*0.1*	44	*72*	/147/	*144*	263**	*65*	95
9510-3	Wh	982	0.842	84.2		15.6	0.1		0.11			3.44	4.6E+28	16	0	n.a.	817	3.1	*2.0*	19	*31*	/64/	*63*	115	*28*	34

Hzb, harzburgite; Lhz, lherzolite; Wh, wehrlite; Ol, olivine; Opx, orthopyroxene; Cpx, clinopyroxene; Spl, spinel; Felds, feldspath; Ap, apatite; Wh, whitlockite; Am, amphibole; Phl, phlogopite. Mg#, $Mg/(Mg+Fe)_{at}$. Petrographic, modal abundances and temperature estimates are after Ionov et al. (2005b, d); *feldspaths host Fe-Ti oxides; density (in g.cm-3) estimated using the method of Lange and Carmichael (1990) for T=940°C at 1.5 GPa; viscosity (Pa.s-1) estimated using methods of Li et al. (2008) and Peslier et al. (2010) assuming P=2.0 GPa. A_{Tot}, total integrated absorbance for olivine, opx and cpx; G1, absorbance for Group 1 OH Band between 3800-3400 cm^{-1}; G2, absorbance for Group 1 OH Band between 3400-3100 cm-1; n.a., not analyzed. [1], measured olivine water contents estimated using Bell et al. (2003) absorption coefficient; [2], estimated olivine water contents calculated assuming equilibrium with cpx, see Table 2; //, estimated cpx and opx water contents calculated assuming equilibrium between cpx and opx, see Table 2; ± (2σ), two sigma error on water estimates; ** water estimates in cpx assuming E//β and E//α are equal.

This is a preprint, the final version is subject to change, of the American Mineralogist (MSA)
Cite as Authors (Year) Title. American Mineralogist, in press.
DOI: https://doi.org/10.2138/am-2020-7316

Table 2 : Partition coefficients, olivine and pyroxenes water content estimates, and melt in equilibrium with pyroxene

		Partition coefficienrts								Water content estimates									
	Rock	$D^{opx/ol}$	$D^{cpx/ol}$	$D^{cpx/opx}$	$D^{opx/melt}$	$D^{cpx/melt}$	$D^{cpx/melt}$	$D^{cpx/opx}$	$D^{cpx/opx}$	Ol_{Eq}	Ol_{Eq}	Ol_{Eq}	± *(2σ)*	Opx_{Eq}	± *(2σ)*	Cpx_{Eq}	± *(2σ)*	H_2O_{MELT}	H_2O_{MELT}
Sample	type	meas	meas	meas	*O10*	*O10, T1*	*O10, T2*	*O10, T1*	*O10, T2*	*N14*	*T09*	av.		av.		av.		T1, ppm	T2, ppm
Lherzolite-harzburgite (LH) series																			
9501-2	Hzb	190	387	2	0.005	0.021	0.014	4	3	36	3.6	20	*33*	67	*66*	139	*136*	0.6	1.0
9506-2	Lhz	95	154	2	0.014	0.029	0.022	2	2	29	2.9	16	*26*	54	*53*	141	*138*	0.3	0.6
9508-31	Hzb	295	693	2	0.006	0.025	0.016	4	3	40	4.0	22	*36*	74	*72*	132	*129*	0.5	0.8
9508-50	Hzb	374	543	1	0.009	0.022	0.017	3	2	38	3.8	21	*34*	70	*68*	202	*198*	0.6	1.2
9510-2	Hzb	70	197	3	0.006	0.026	0.017	5	3	91	9.1	50	*82*	168	*164*	249	*244*	1.1	1.4
9510-4	Hzb	109	248	2	0.006	0.022	0.015	4	2	72	7.2	40	*65*	133	*130*	247	*242*	1.1	1.7
9510-8	Hzb	68	139	2	0.007	0.024	0.017	3	2	46	4.6	26	*42*	86	*84*	176	*173*	0.6	1.0
9510-16	Lhz	119	165	1	0.007	0.023	0.016	3	2	35	3.5	19	*31*	64	*62*	193	*189*	0.5	1.2
9510-19	Hzb	269	381	1	0.008	0.019	0.013	2	2	30	3.0	17	*27*	55	*54*	165	*161*	0.5	1.3
average				*2*	*0.008*	*0.023*						*26*	*23*						
Lherzolite-wehrlite (LW) series																			
9503-2	Lhz	33	76	2	0.019	0.034	0.024	2	1	34	3.4	19	*31*	63	*61*	115	*113*	0.3	0.5
9510-11	Lhz	154	441	3	0.007	0.027	0.018	4	3	52	5.2	29	*47*	96	*94*	141	*138*	0.6	0.8
9502-1	Wh	9	16	2	0.006					3	0.3	2	*3*	6	*5*	13	*13*		
9510-1	Wh	460	822	2	0.009	0.035	0.026	4	3	80	8.0	44	*72*	147	*144*	346	*338*	0.7	1.4
9510-3	Wh		37		0.007	0.023	0.017	3	2	35	3.5	19	*31*	64	*63*			0.5	0.0
average								*3*	*2*			*22*	*15*					*0.6*	*1.0*
standard deviation								*2*	*1*									*0.5*	*0.9*

$D^{px/melt}$ partition coefficient between opx or cpx with melt; $D^{opx/melt}$ = exp(-5.66+8.4[IVAl]opx +10[Ca]opx); $D^{cpx/melt}$ = exp(-5+6.3[IVAl]cpx -1.2[Ca]cpx+1600/T); T1, Temperature of equilibation; T2, 1200˚C; meas, partition coefficient calculated using measured water contents in minerals; O10, partition coefficient between opx and cpx with melt using method of O'Leary et al (2010). Ol_{Eq}, Opx_{Eq}, Cpx_{Eq} olivine, opx and cpx water contents calculated using partition coefficient. N14, partition coefficient of Novella et al (2014); T09, partition coefficient of Tenner et al (2009), av., average of olivine, opx and cpx water content estimates using partition coefficients. H_2O_{MELT}, water contents estimate of potential metasomatic agent with the cpx using $D^{cpx/melt}$ of O'Leary et al (2010)

977

This is a preprint, the final version is subject to change, of the American Mineralogist (MSA)
Cite as Authors (Year) Title. American Mineralogist, in press.
DOI: https://doi.org/10.2138/am-2020-7316

Fig. 1

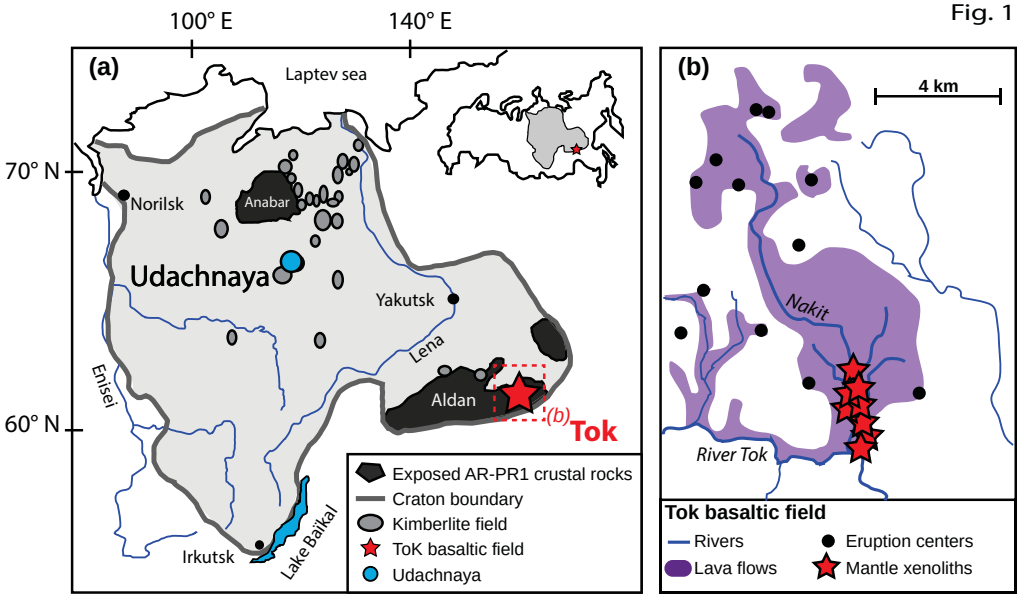

This is a preprint, the final version is subject to change, of the American Mineralogist (MSA)
Cite as Authors (Year) Title. American Mineralogist, in press.
DOI: https://doi.org/10.2138/am-2020-7316

Fig. 2

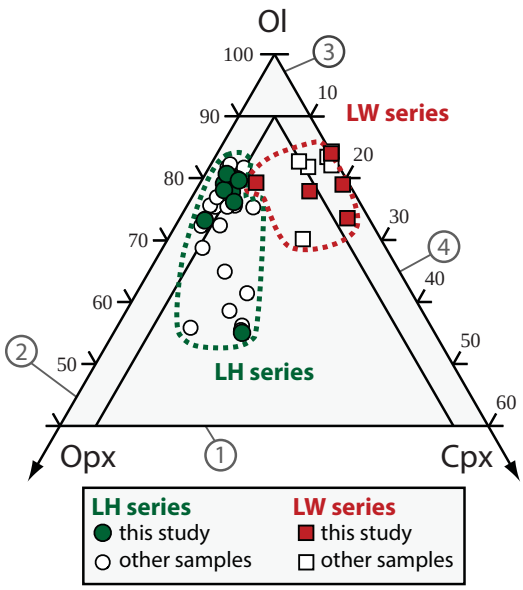

This is a preprint, the final version is subject to change, of the American Mineralogist (MSA)
Cite as Authors (Year) Title. American Mineralogist, in press.
DOI: https://doi.org/10.2138/am-2020-7316

Fig. 3

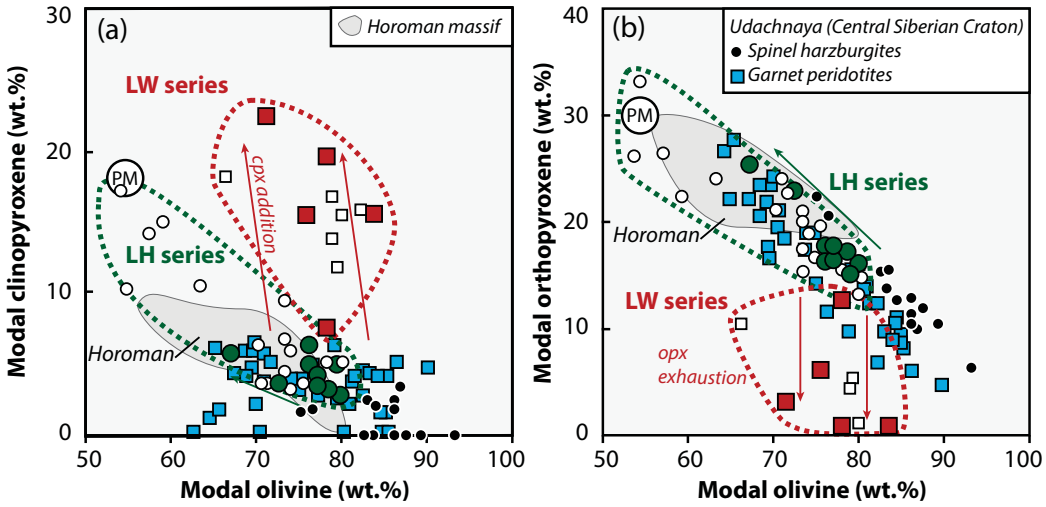

This is a preprint, the final version is subject to change, of the American Mineralogist (MSA)
Cite as Authors (Year) Title. American Mineralogist, in press.
DOI: https://doi.org/10.2138/am-2020-7316

Fig. 4

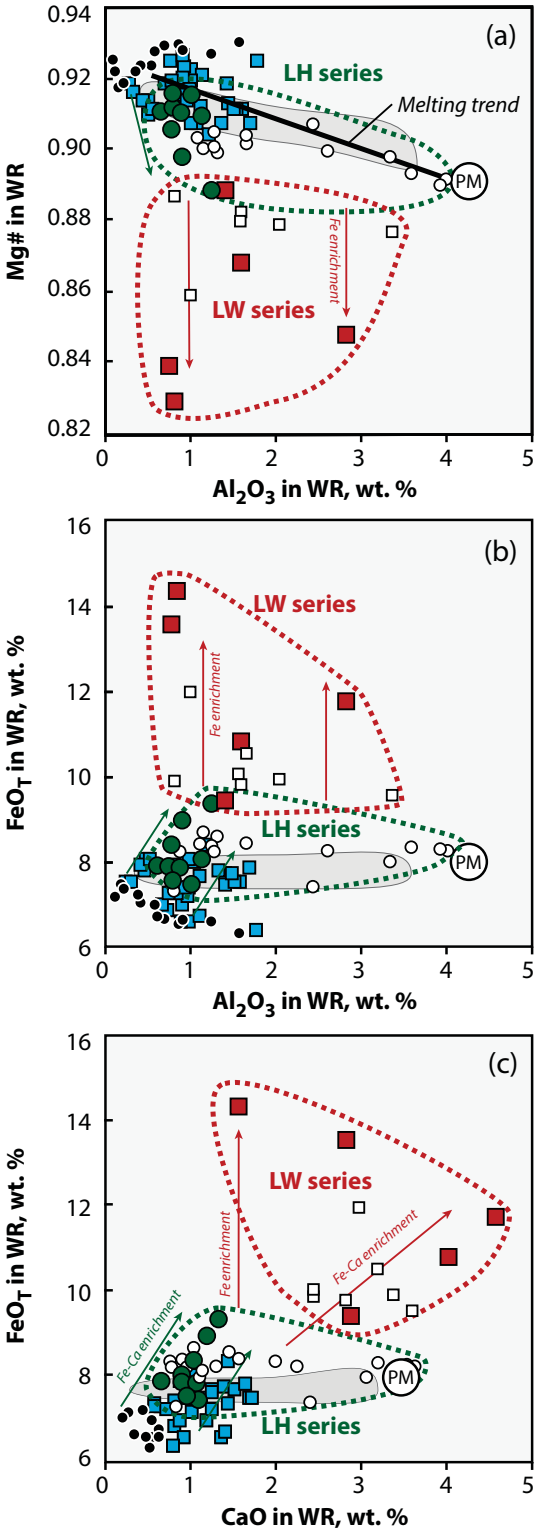

This is a preprint, the final version is subject to change, of the American Mineralogist (MSA)
Cite as Authors (Year) Title. American Mineralogist, in press.
DOI: https://doi.org/10.2138/am-2020-7316

Fig. 5

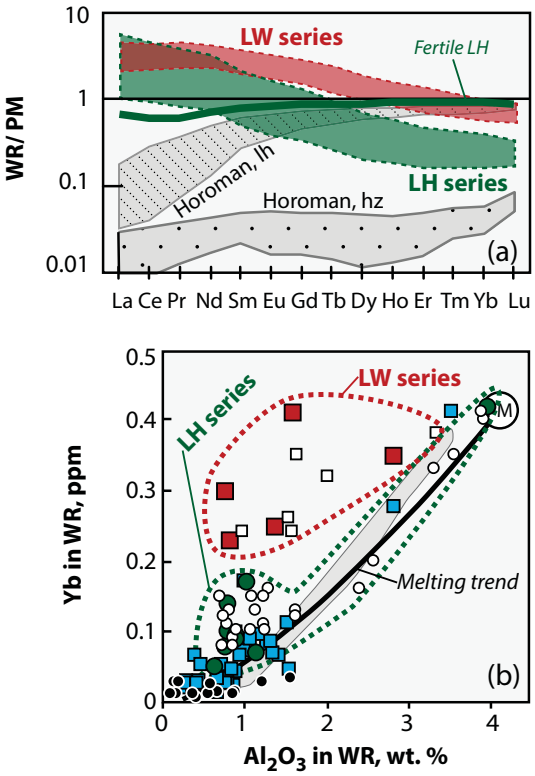

This is a preprint, the final version is subject to change, of the American Mineralogist (MSA)
Cite as Authors (Year) Title. American Mineralogist, in press.
DOI: https://doi.org/10.2138/am-2020-7316

Fig. 6

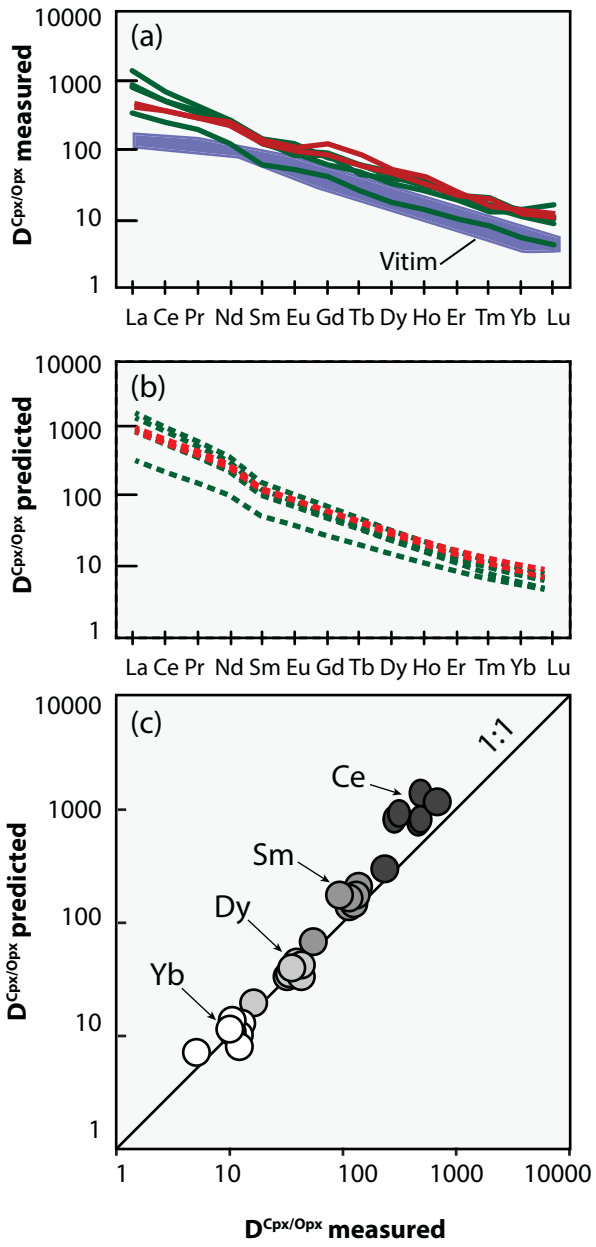

This is a preprint, the final version is subject to change, of the American Mineralogist (MSA)
Cite as Authors (Year) Title. American Mineralogist, in press.
DOI: https://doi.org/10.2138/am-2020-7316

Fig. 7

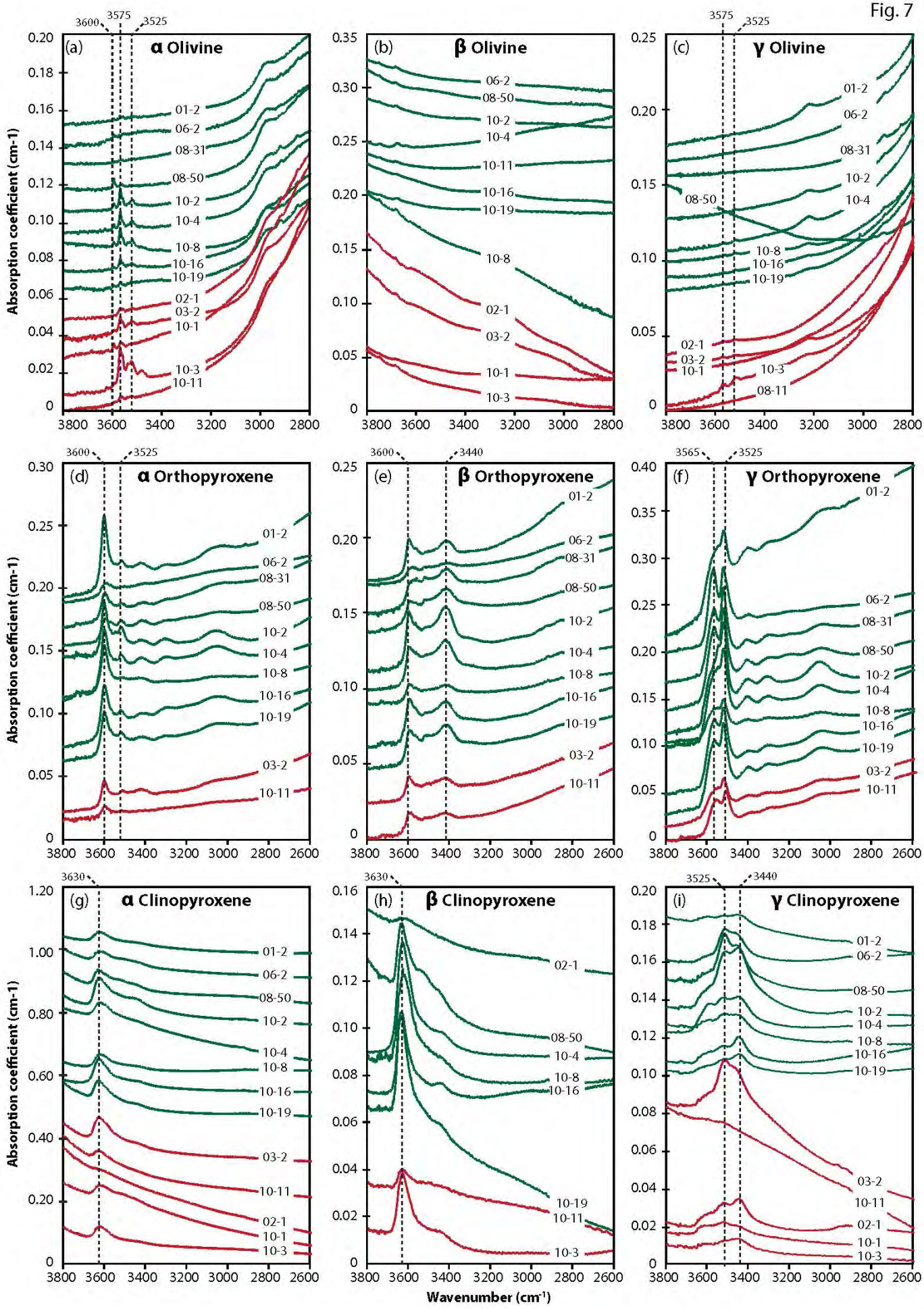

This is a preprint, the final version is subject to change, of the American Mineralogist (MSA)
Cite as Authors (Year) Title. American Mineralogist, in press.
DOI: https://doi.org/10.2138/am-2020-7316

Fig. 8

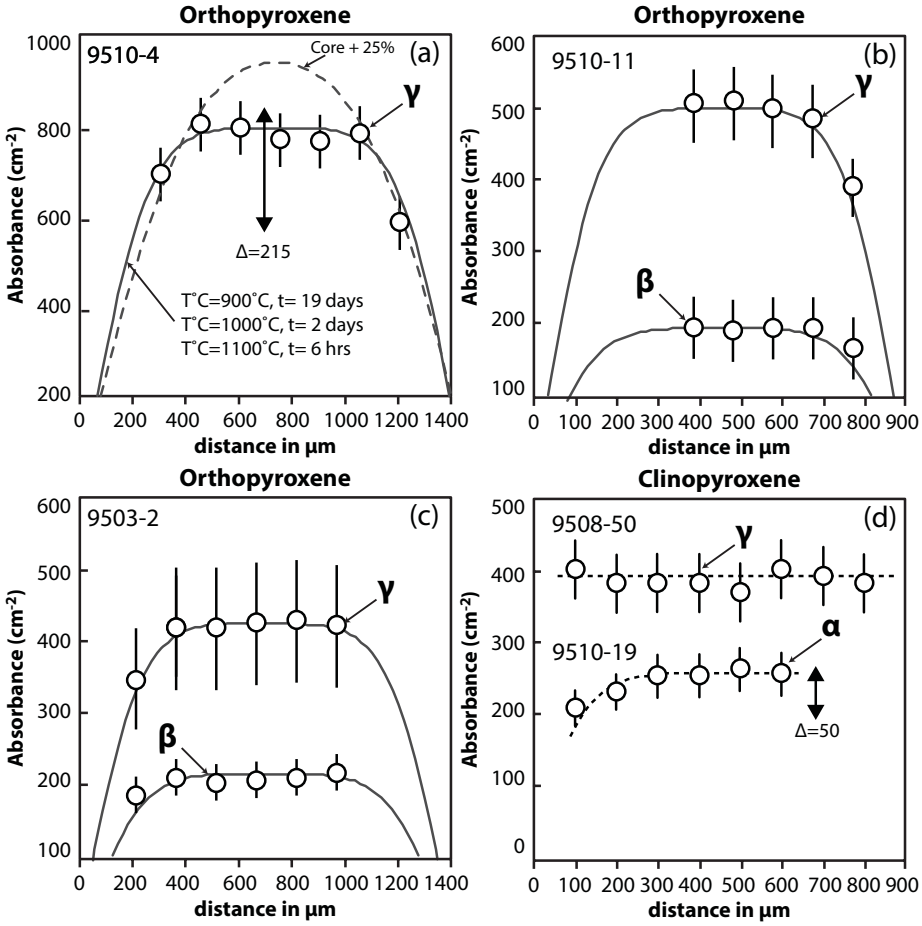

This is a preprint, the final version is subject to change, of the American Mineralogist (MSA)
Cite as Authors (Year) Title. American Mineralogist, in press.
DOI: https://doi.org/10.2138/am-2020-7316

Fig. 9

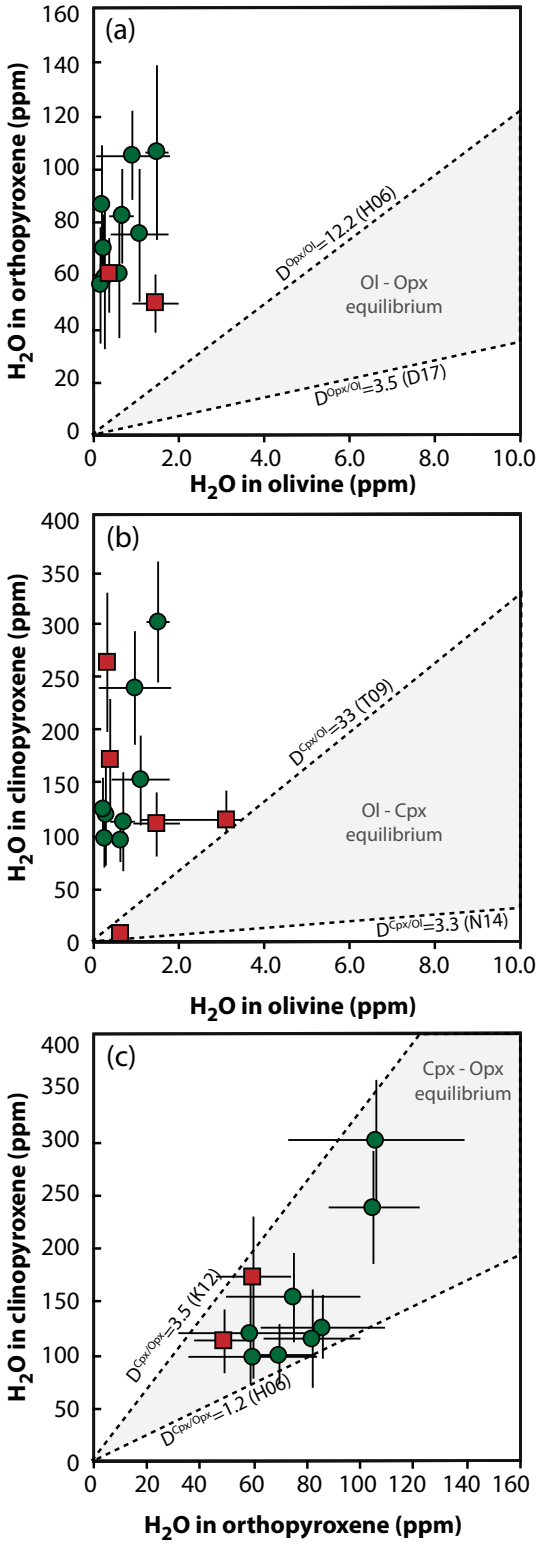

This is a preprint, the final version is subject to change, of the American Mineralogist (MSA)
Cite as Authors (Year) Title. American Mineralogist, in press.
DOI: https://doi.org/10.2138/am-2020-7316

Fig. 10

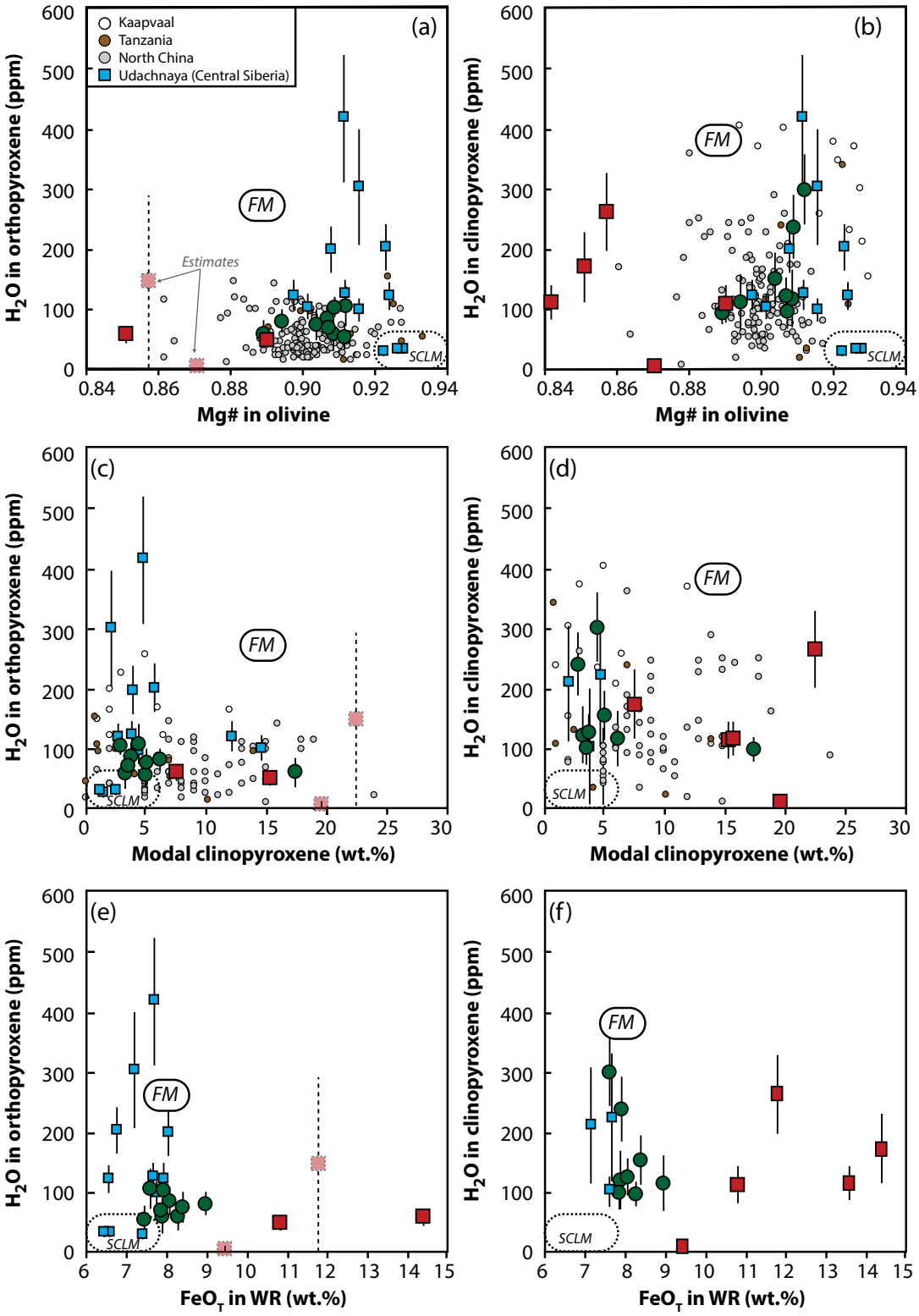

This is a preprint, the final version is subject to change, of the American Mineralogist (MSA)
Cite as Authors (Year) Title. American Mineralogist, in press.
DOI: https://doi.org/10.2138/am-2020-7316

Fig. 11